ACCSCIENCE PUBLISHING

Engineering Science in Additive Manufacturing

ORIGINAL RESEARCH ARTICLE

Laser sequence and build orientation govern interface quality in multi-material laser powder bed fusion

Jacklyn Griffis[1,2], Aishwarya Deshpande[1], Bryan Gong[1], Kazi Shahed[3], Avez Shaikh[1], Jeremy Schreiber[2], and Guha Manogharan[1,3]*

[1]Department of Mechanical Engineering, College of Engineering, Pennsylvania State University, Pennsylvania, United States of America

[2]Applied Research Laboratory at Pennsylvania State University, Pennsylvania, United States of America

[3]Department of Industrial and Manufacturing Engineering, College of Engineering, Pennsylvania State University, Pennsylvania, United States of America

Abstract

Multi-material laser powder bed fusion (MM-LPBF) offers the ability to locally tailor functional properties by combining dissimilar metals within a single component. However, achieving robust bonding at highly mismatched interfaces remains a critical challenge. This work investigates the interfacial evolution in CuCrZr–316LSS transitions, a material pair with extreme differences in thermal conductivity and a 75% difference in optimal volumetric energy density. This study investigates the interfacial formation mechanisms in CuCrZr–316LSS using five distinct interface configurations: (i) 316L deposited over CuCrZr across a horizontal interface, (ii) CuCrZr deposited over 316L across a horizontal interface, (iii) 316L deposited over CuCrZr along a diagonal interface, (iv) CuCrZr deposited over 316L along a diagonal interface, and (v) the two materials printed with a vertical interface via intralayer deposition. The results demonstrate that deposition order, i.e., laser scanning sequence, and interface geometry critically dictate the quality of interfaces in MM-LPBF systems. Microstructural characterization via optical microscopy, scanning electron microscopy, energy-dispersive X-ray spectroscopy, electron backscatter diffraction, and transmission electron microscopy revealed that exposure sequence strongly governs interfacial morphology, phase development, and the presence of interfacial defects. To further contextualize these results, meso-scale computational fluid dynamics simulations were employed to capture melt-pool dynamics, convection patterns, and material mixing behavior. Overall, this work clarifies the fundamental role of build orientation and laser scanning sequence in governing process stability and interface quality in MM-LPBF systems (copper- and iron-based in this study) and lays the foundation to achieve reliable interface quality in multi-material components manufactured through MM-LPBF.

Keywords: Laser scan strategy; Build orientation; Dissimilar metal interfaces; Multi-material additive manufacturing; Multi-material laser powder bed fusion; Process simulation; Selective powder deposition

***Corresponding author:**
Guha Manogharan
(gum53@psu.edu)

Citation: Griffis J, Deshpande A, Gong B, *et al*. Laser sequence and build orientation govern interface quality in multi-material laser powder bed fusion. *Eng Sci Add Manuf*. 2026;2(4):026360018. doi: 10.36922/ESAM026360018

Received: September 1, 2026

Revised: September 16, 2026

Accepted: September 29, 2026

Published online: October 26, 2026

Copyright: © 2026 Author(s). This is an Open-Access article distributed under the terms of the Creative Commons Attribution License, permitting distribution, and reproduction in any medium, provided the original work is properly cited.

Publisher's Note: AccScience Publishing remains neutral with regard to jurisdictional claims in published maps and institutional affiliations.

1. Introduction

Laser powder bed fusion (LPBF) is a well-adopted additive manufacturing (AM) technology due to its capability to produce high-resolution, complex, and high-performance metal components directly from digital models. Recent advances have expanded the capabilities of LPBF to multi-material LPBF (MM-LPBF) using selective powder deposition (SPD), enabling the fabrication of components comprising distinct material systems with tailored mechanical, thermal, and functional properties within a single manufacturing process.[1–4] For example, triply periodic minimal surfaces, where both the advantages of AM and MM-LPBF are applicable and well realized.[5–7]

Recent technological advancements in SPD have introduced both opportunities and challenges, particularly in the AM of multi-metallic interfaces. The ability to achieve selective (i.e., voxel-based) deposition of multiple material systems provides high-resolution (<300 μm) control to achieve distinct material interfaces, along with the ability to achieve finer part feature resolution and complex geometries (i.e., like single-material LPBF).

Hence, both the processing regime and part properties of MM-LPBF are significantly different from functionally graded material (FGM) achieved through directed energy deposition (DED[8,9]) which has a gradual gradation of composition at higher volumetric energy density and coarser design features that are typically deployed for large geometries and repair applications.[10,11]

In short, the orientation of the multi-material interface relative to the build platform significantly impacts the thermal histories at the multi-metallic interface, which in turn affects metallurgical bonding between dissimilar materials in both MM-LPBF[12] and FGM-DED. Furthermore, material mixing at the interfaces dictates the interface morphology, which directly impacts the microstructure evolution and the potential formation of thermodynamically stable intermetallic or solid-solution phases.

In recent years, there has been a growing demand to achieve new manufacturing capability where material systems with extreme differences in intrinsic properties (e.g., mechanical and thermal characteristics) can be engineered for the design and manufacturing of components for high-performance applications.[13,14] MM-LPBF process offers the ability to realize this manufacturing need; however, the underlying AM processing science and resulting structure–property relationship at the MM-LPBF interface have not been well understood, which is the motivation for this study.

For example, copper-based alloys (e.g., CuCrZr) have gained substantial attention within aerospace, fusion reactors, electronic cooling, and other high-performance applications due to their relatively superior thermal conductivity, electrical conductivity, and commendable mechanical properties at elevated temperatures compared to pure copper.[15] The rapid cooling inherent to the LPBF process allows for effective supersaturation and precipitation of nano-sized chromium and zirconium phases, which results in improved hardness, tensile strength, and electrical conductivity without sacrificing thermal conductivity relative to conventionally processed alloys.[16] In the aerospace sector, CuCrZr is particularly valuable for applications that involve high thermal loads, such as regeneratively cooled rocket engine components. A recent study discussed the use of CuCrZr in these extreme environments, noting its superior thermal conductivity and resistance to thermal fatigue, which are critical for sustaining high heat fluxes during engine operation.[16] However, most applications often desire combining CuCrZr with auxiliary structural material systems with complementary mechanical and corrosion-resistance characteristics, such as austenitic stainless steels (e.g., 316LSS).

However, prior studies have reported that it is inherently challenging to combine these material systems due to their significant differences in melting temperature, thermal expansion coefficients (CTE), and diffusivity, as well as the presence of a miscibility gap in the iron–copper system.[17,18] The immiscibility gap between iron and copper can lead to the formation of complex, heterogeneous microstructures, including copper-rich micro-segregation, porosity, and solidification cracks, which can severely impact the mechanical performance of the part.[19,20]

Prior research on MM-LPBF interfaces of CuCrZr and 316LSS has primarily explored processing parameters,[21] residual stress effects,[22] and mechanical properties. Other studies have proposed several strategies for mitigating defect formation, such as beam shaping,[23] intermediate transition layers,[24] surface treatments,[25] and post-processing techniques like hot isostatic pressing.[26] One of these studies highlighted that laser beam shaping significantly impacts the microstructural integrity and defect formation when printing CuCrZr onto 316LSS substrates.[23] Specifically, ring-mode laser beams resulted in reduced porosity and more defined interfaces compared to Gaussian beams, suggesting superior microstructural control through tailored energy distribution. Another study employed coupled thermal-mechanical simulations with experimental observations and reported that residual stress at the alloy interfaces directly correlated with increased scanning speeds and subsequent cracking susceptibility.[22] In a recent study, it was reported that the CTE mismatch

and residual stress gradients predominantly caused cracking within the 316LSS when the two materials are printed at a vertical interface using intralayer deposition, emphasizing the need for targeted processing conditions to mitigate thermal expansion disparities.[17]

A summary review of relevant literature on MM-LPBF of CuCrZr-316LSS is presented in Table 1. It should be noted that there is a critical gap in the understanding of interface quality when such extreme material systems are processed within a single layer (i.e., intra-layer), and when fundamental questions remain unanswered regarding the effects of build orientation and laser scanning strategies on the interface integrity of these materials, especially through selective powder deposition (i.e., intra-layer) during MM-LPBF processes.

In summary, advancements in the processing capabilities of MM-LPBF to fabricate dissimilar material interfaces within a single build without the constraints of traditional casting or welding methods can help realize significant advantages in producing lightweight, high-performance multi-material components.

Table 1. Review of literature on the multi-material laser powder bed fusion interfaces between CuCrZr, 316LSS, and related material systems

Material pair and reference	Evaluation methods	Specimen design and build direction	Key findings and observations
AISI 316LSS/16MgCr5 & CuCrZr & Al-Sc/AlSi10Mg[17]	Microstructural: neutron tomography, OM, and EDS; mechanical: tensile testing and fractography	CuCrZr over 316LSS	• Cracks were perpendicular to the interface and present in the steel volume, which was attributed to differences in CTE mismatch and residual stress in the steel. Tensile bars fractured in the CuCrZr volume
CurZr & 316LSS[18]	Microstructural: OM, SEM, and EDS; mechanical: N/A	Intra-layer orientation and design of experiments included scanning strategy	• Intralayer deposition method required vacuuming unmelted powder on each layer to enable material changes, thereby minimizing cross-contamination between materials prior to laser exposure • Laser scan sequence impacts interface crack formation. Cracks emerged when 316LSS was processed first due to higher temperature gradients and CTE mismatch causing elevated thermal stress • Scanning across interfaces was effective in reducing cracks and resulted in a larger diffusion zone
CuCrZr & 316LSS[19]	Microstructural: OM; mechanical: simulation: DEM for powder spreading and CFD in ANSYS FLUENT	316LSS over CuCrZr and CuCrZr over 316LSS	• Recoil pressure and Marangoni convection contributed to the mixing of 316LSS and CuCrZr • As scanning speed decreases or power increases, a longer molten pool lifetime was observed, which increased the immiscibility of the mixture • Larger numbers of CuCrZr islands were formed inside the molten pool at higher energy density with improved homogeneity • CuCrZr grains grew along the boundary in the molten pool and were inhibited by the solidified 316LSS, resulting in finer equiaxed grains at the interface
CuCrZr & 316LSS[20]	Microstructural: OM, SEM, EDS, and EBSD; mechanical: tensile with DIC, microhardness, fractography	316LSS over CuCrZr	• Tensile fractures in CuCrZr at loads were reported to be similar to single-material specimens • Cracks at the interface, primarily in 316LSS along the high-angle grain boundaries, were attributed to immiscibility of the Fe–Cu system, which caused the Cu to segregate at the grain boundaries
CuCrZr & 316LSS[21]	Microstructural: OM; mechanical: tensile and hardness	Steel over CuCrZr only in inter-layer orientation	• Studied the effect of laser VED on interfacial hardness and tensile strength when depositing 316LSS on CuCrZr • As VED increased, melt pool size gradually expanded, cooling time increased, and the degree of alloying at the interface increased
CuCrZr & 316LSS[22]	Microstructural: OM; mechanical: N/A; simulation: thermo-mechanical FEA using MOOSE software	316LSS over CuCrZr and CuCrZr over 316LSS	• Higher residual stress at the interface was proposed to be due to scanning speed • Cracks at the interface are attributed to excessive residual stress

(*Cont'd...*)

Table 1. (*Continued*)

Material pair and reference	Evaluation methods	Specimen design and build direction	Key findings and observations
CuCrZr & 316LSS[23]	Microstructural: OM, SEM (BSE), EBSD, and EDS; mechanical: N/A	316LSS baseplate with CuCrZr cubes	• Beam shaping affected microstructure, texture, and defects in dissimilar materials • Ring-mode laser induced smaller BCC fractions compared to Gaussian beam • Ring-mode laser led to sharper interfaces with less porosity and less intense cracking • Gaussian beam led to more equiaxed grains in CuCrZr due to higher Fe dissolution
316LSS & CuCrZr interface via In718[24]	Microstructural: OM, SEM, EDS, EBSD, and TEM; mechanical: tensile tests for SS-IN, IN-Cu, and SS-IN-Cu specimens, and flexural testing	400 μm thick (10-layer) transition layer. Only inter-layer: 316LSS à In718 à CuCrZr	• Good bonding with dendritic grains at the In718-SS interface, with an interface width of 500 μm, was observed • Keyhole pores at the In718-CuCrZr interface were observed and were attributed to nucleation points of equiaxed Cu grains due to a higher cooling rate at the interface • Macroscopic defects were not observed at the SS-In-CuCrZr interface, with complete elemental diffusion • The In718 transition layer has large strain at the SS interface. In718-CuCrZr transition has finer grains • SS-In718-CuCrZr samples fractured in the CuCrZr volume
CuCrZr & 316LSS[25]	Microstructural: OM, SEM, EDS, EBSD, and XRD; mechanical: tensile, hardness, and fractography.	SS substrate with single material CuCrZr in inter-layer-only orientation	• Examined the effects of substrate surface finishing on interface mechanical strength for material changes along the vertical direction • Small holes and perpendicular cracks were observed at the interface • XRD showed the absence of intermetallic compounds
CuCrZr & 316LSS[26]	Microstructural: OM, SEM, EDS, and EBSD; mechanical: nanoindentation	Concentric cuboids with CuCrZr embedded inside 316LSS cubes. Design of experiments included melted and unmelted CuCrZr powder separated from the materials	• Manufactured using an Aerosint SPD recoater (as reported in this study) • Recommended that post-AM HIP could be effective in healing cracks and pores at the interface • Hardness of the CuCrZr closer to the interface was higher than bulk Cu due to the strengthening effect of the fine Fe particles formed by spinodal decomposition and localized fine grain size • After HIP, an overall decrease in hardness in CuCrZr was observed • Grain refinement of CuCrZr at the interface was observed • Unmelted CuCrZr powder at the interface resulted in similar mechanical properties after HIP • Required all interfaces to be enclosed/internal for HIP processing
CuCrZr & 316LSS[27]	Microstructural: N/A; optical imaging of specimens without any microscopy or other characterization; mechanical: N/A	Cubes in all orientations, overhanging bars (Single material), wall bars (Single material), voxel-type graded interface, some complex geometries	• Manufactured using Aerosint SPD recoater (like the study reported in this article) • Recommended design guidelines for orienting part on build plate to reduce thermal build-up (all guidelines were not MM-LPBF specific)
CuCrZr & 316LSS[28]	Microstructural: OM, SEM, and EDS; mechanical: tensile, fractography, and hardness	CuCrZr over 316LSS in inter-layer-only orientation	• Micro-segregation (in islands and spherical phases) caused by the miscibility gaps in the 316LSS volume was reported • Micro-cracks distributed in the 316LSS volume with unfused powders and pores were observed in the CuCrZr volume • Gradual hardness change across interface and tensile fracture occurred in the CuCrZr volume

Abbreviations: AM: Additive manufacturing; BCC: Body-centered cubic; BSE: Backscattered electron; CFD: Computational fluid dynamics; CTE: Coefficient of thermal expansion; DEM: Discrete element method; DIC: Digital image correlation; EBSD: Electron backscatter diffraction; EDS: Energy-dispersive X-ray spectroscopy; FEA: Finite element analysis; HIP: Hot isostatic pressing; LPBF: Laser powder bed fusion; MOOSE: Multiphysics Object-Oriented Simulation Environment; N/A: Not available; OM: Optical microscopy; SEM: Scanning electron microscopy; SPD: Selective powder deposition; SS: Stainless steel; TEM: Transmission electron microscopy; VED: Volumetric energy density; XRD: X-ray diffraction.

Computational fluid dynamics (CFD) analyses have emerged as a critical tool for understanding melt-pool behavior and interfacial evolution in both single-material[29] and multi-material LPBF.[30] Meso-scale CFD simulation provides insights into thermo-fluidic dynamics, laser-induced heat, and mass transfer within the melt pool to provide quantitative predictions of melt pool shape, stability, mixing behavior, thermal history, and defect formation.[31] Chen *et al.*[32] applied a CFD-based model to study In625/SS316L FGM-DED transitions and observed that counterclockwise directional Marangoni circulation governs whether intermixed or unmixed regions develop at the interface and that the direction of melt pool mixing is highly dependent on the material systems. Sun *et al.*[30] demonstrated the value of discrete element method (DEM)–CFD coupling in simulating mesoscale melt-pool morphology in inter-layer In718/Cu10Sn LPBF and reported that differences in thermal conductivity and absorptivity strongly dictate melt-pool continuity and temperature distributions.

More relevant to the iron–copper-based system (employed in this study), Gu *et al.*[33] extended the DEM approach to 316LSS/Cu10Sn systems to include experimental evaluation. It was reported that vertically deposited bimetallic configurations produce discontinuous melt pools due to the relatively high thermal conductivity of copper-based alloys, while horizontal arrangements exhibit convection-assisted mixing as molten 316LSS transports heat into adjacent CuSn10 volumes. In short, these studies demonstrate that CFD and other computational simulation techniques are garnering interest in their application to predict process stability, interfacial mixing, defect formation, and printability in dissimilar-metal systems where thermal property disparities could drive the fundamental physics of melt-pool behavior.

It is well known that build direction in LPBF can impact the heat flow during the processing stages by influencing melt-pool composition, solidification rates, grain structure, and interfacial defect formation. Previous work has demonstrated the influence of build orientation on interface formation and defect evolution.[2] Specifically, research involving CuSn10 and 904LSS using MM-LPBF indicated that orientation was strongly correlated with the resulting microstructure, residual stresses, thermal gradients, and mechanical properties, all of which influence the overall mechanical performance.

In this study, the substantial thermal diffusivity contrast between CuCrZr and 316LSS is evidenced by the increased difference in laser processing volumetric energy density (VED). In this material pair, there is a ~75% difference in optimal VED, compared to the ~20% difference investigated in prior work related to the MM-LPBF processing of iron–copper systems. As a result, build orientation is anticipated to play an exaggerated role in determining interfacial formation mechanisms. Understanding how build direction contributes to these phenomena in MM-LPBF is critical for improving the design and fabrication of components for high-performance applications.

In this investigation, we systematically evaluate how build orientation affects the bonding mechanisms at the interface of extremely thermally contrasting alloy pairing in MM-LPBF, CuCrZr-316LSS, using a multi-scale characterization approach. Leveraging advanced characterization techniques, including nanoindentation and transmission electron microscopy (TEM) for sub-micron-scale analysis, scanning electron microscopy (SEM), energy-dispersive X-ray spectroscopy (EDS), and electron backscatter diffraction (EBSD, as well as optical microscopy for macroscale observations, we aim to elucidate the relationships between orientation, microstructure evolution, and resulting mechanical properties. CFD simulations using FLOW-3D will provide additional insights into the fundamental understanding of laser powder interactions during melt-pool evaluation in MM-LPBF. Our findings will provide essential insights to achieve ideal MM-LPBF processing strategies for robust, multi-material metallic interfaces critical to advanced manufacturing applications.

2. Methods and materials

2.1. Fabrication and preparation

As shown in Figure 1, microscopy cubes (1 cm^3) were printed in five unique interface orientations to determine the effect of build orientations on the formation mechanisms of the interface between materials of highly contrasting thermal properties. All specimens were fabricated on an Aconity MIDI+ (Aconity3D GmbH, Germany) equipped with an Aerosint SPD (Aerosint SA, Belgium) with a single-mode fiber laser at a continuous wavelength of 1,070 nm and an effective spot size of 80 μm. Since 316LSS and CuCrZr have vastly different thermal properties and optical absorption of infrared light, distinct laser processing parameters were used for each material subsection in a layer-wise fashion. Material-specific laser parameters are presented in Table 2. A sequential laser scanning strategy was used for each layer, where CuCrZr powder was melted first, followed by the 316LSS volume. The interlayer rotation was set to 90° and the build chamber was flushed with inert argon gas, and oxygen concentrations were kept below 800 ppm. Powder feedstock compositions

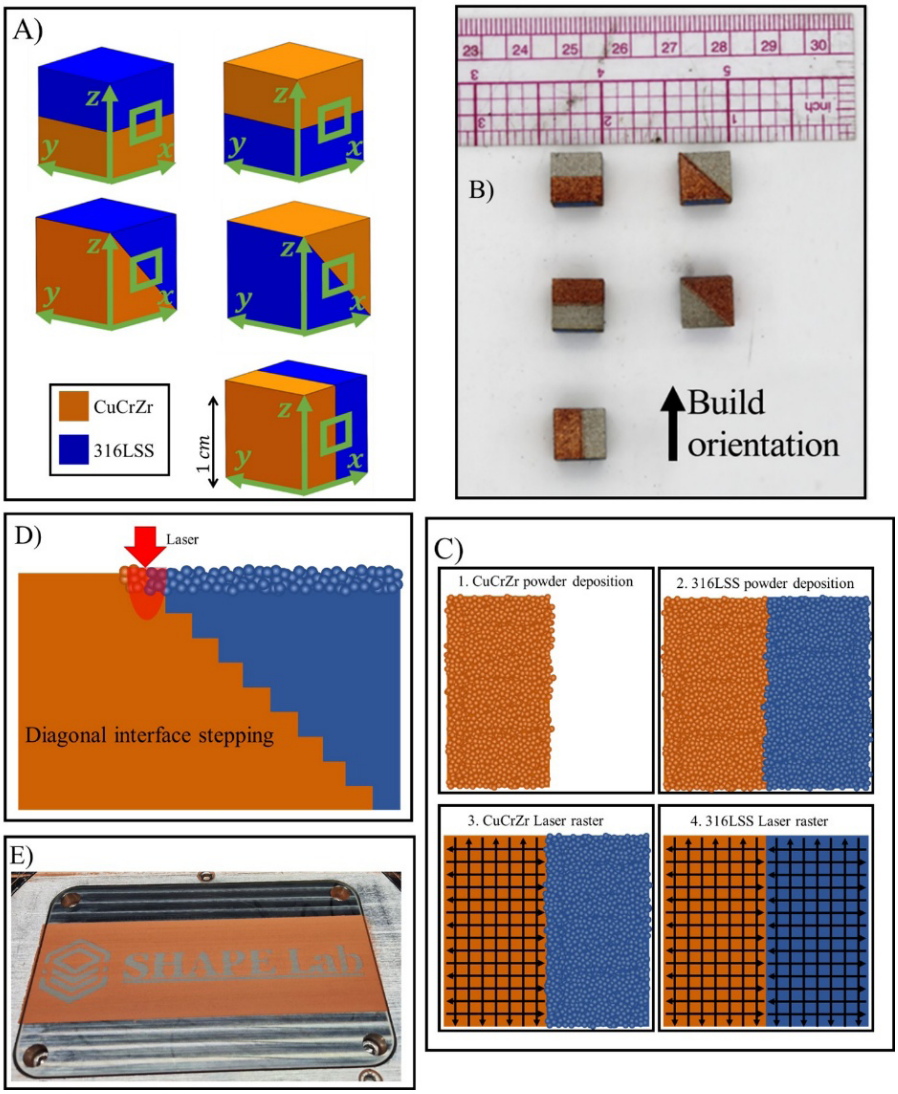


Figure 1. Multi-material laser powder bed fusion (MM-LPBF) fabrication strategy and build-orientation configurations for CuCrZr–316LSS interfaces. (A) Five fundamental build orientations investigated, manufactured from CuCrZr (Orange) and 316LSS (Blue) using MM-LPBF. (B) As-built microscopy cubes. (C) Order of layer-wise powder deposition and laser exposure for intralayer deposition. (D) Interface stair stepping for diagonal interfacial orientations. (E) Sample powder deposition.

presented in Tables 3 and 4 are provided by the suppliers Thyssenkrupp Material Trading (GmbH, Germany) and Eckart TLS (GmbH, Germany), respectively.

These samples were electron discharge machined off the build plate, hot-mounted in epoxy, and polished up to a 0.04 µm colloidal silica solution for subsequent microstructural, crystallographic, and chemical composition analysis using numerous techniques across multiple length scales.

$$VED = \frac{P}{vht} \quad (1)$$

2.2. Nanoindentation

Young's modulus and hardness were measured with a nanoindenter (Hysitron TI 950, United States) fitted with a Berkovich tip. Two locations well within CuCrZr and 316LSS volumes, where there was no contamination from the other material, were characterized for bulk constituent material properties. The third location was selected within a well-mixed area along the interface, with a minimum of three random representative measurements taken in each location. Indentation was conducted at a maximum cutoff load of 10 mN and a dwell time of 2 seconds. The Hysitron TriboScan (10.2.0.1, Hysitron, United States) software

Table 2. List of laser processing parameters by material, where volumetric energy density is presented in Equation 1

Material	Power (P)	Scanning speed (v)	Hatch spacing (h)	Layer thickness (t)	Volumetric energy density (VED)
Units	[W]	$\left[\frac{mm}{s}\right]$	$[\mu m]$	$[\mu m]$	$\left[\frac{J}{mm^3}\right]$
CuCrZr	500	600	120	40	173.61
316LSS	150	600	80	40	78.13

Table 3. 316LSS powder composition sourced from Thyssenkrupp Material Trading[34]

Composition (wt.%)	Ferum	Carbon	Silicon	Manganese	Phosphorus	Sulfur	Chromium	Nickel	Nitrogen	Molybdenum
316LSS	Balance	0.03	1.00	2.00	0.045	0.015	16.50–18.50	10.00 – 13.00	0.10	2.00–2.50

Table 4. CuCrZr powder composition sourced from Eckart TLS[35]

Composition (wt.%)	Copper	Chromium	Zirconium	Ferum	Silicon
CuCrZr	Balance	0.50–1.20	0.03–0.3	≤ 0.08	≤ 0.10

was used to deduce the slope of the unloading curve and compute the reduced Young's modulus (E_r). The sample Young's modulus was then calculated based on the Oliver and Pharr method.[36]

2.3. Microscopy characterization through scanning electron microscopy with energy-dispersive X-ray spectroscopy and electron backscatter diffraction

Scanning electron microscopy, EDS, and EBSD were performed to characterize the microstructure, chemical composition, and grain size distribution of the interfaces (Apreo, Thermo Fisher Scientific, United States). EBSD Euler maps determined the shape, size, and local distribution of grains across the interfaces. EDS provides elemental alloy distribution on the fusion plane. SEM was performed at an operating voltage of 20 kV and an amperage of 3.2 nA at a working distance of 2–5 mm (Apreo, Thermo Fisher Scientific, United States). Kernel average misorientation (KAM) maps were generated to provide an indication of local grain misorientations and are often used to represent strain distribution. All post-processing of raw EBSD data was completed using Aztec (version 6.3, Oxford Instruments, United Kingdom) and AztecCrystal 4.0 software (build 4.0.529, Oxford Instruments, United Kingdom).

Electron backscatter diffraction line scans were performed across the bi-material interfaces for all five build orientation coupons. For each orientation, EDS line scans ($n = 8$ per sample) were collected at similar locations and averaged to reduce local variability. The interfacial width was estimated by measuring the distance between the copper and iron elemental intensity plateaus.

2.4. Crystallographic orientation through X-ray diffraction

A Malvern PANalytical Empyrean X-ray diffractometer (XRD) with a copper source, equipped with a 1-der detector, was used to study crystallinity and phase composition across the interface of all five orientations. 2θ scans were conducted from 35° to 100° at a working voltage of 45 kV and amperage of 40 mA. All curves were representative of a face-centered cubic (FCC) crystal structure associated with $\gamma - 316LSS$ and pure-copper phases.

The full width at half maximum (FWHM) and peak positions were determined through peak profile fitting using PANalytical Data Viewer software (version 2.4, Malvern PANalytical, United Kingdom). Crystallite size was subsequently estimated using the Scherrer equation,[37] which assumes that peak broadening arises primarily from instrumental effects and finite crystallite size, with negligible contributions from microstrain. To assess this assumption, conventional Williamson–Hall analysis was performed; however, the resulting negative slopes yielded nonphysical microstrain estimates.[38,39] Consequently, microstrain contributions were neglected in the crystallite size calculations. Importantly, neglecting microstrain

associated with local lattice distortions does not imply the absence of macroscopic residual stresses induced during the MM-LPBF process.

$$D = \frac{K\lambda}{\beta\cos(\theta)} \quad (2)$$

where β is the FWHM, θ is the Bragg angle, K is the Scherrer constant (0.9), λ is the X-ray wavelength, and D is the average crystallite size. A size-only estimate of dislocation density (ρ) can be calculated using **Equation 3**.

$$\rho = \frac{1}{D^2} \quad (3)$$

2.5. Intragranular inclusions via transmission electron microscopy

Transmission electron microscopy and scanning TEM with EDS (STEM-EDS) were performed using a Thermo Fisher Talos TEM operated at an accelerating voltage of 200 kV. High-angle annular dark-field STEM imaging was used to provide enhanced atomic number (Z) contrast, with image intensity proportional to Z,[2] which illustrated distinct differentiation of compositional variations across the bi-material interface when compared to conventional TEM. STEM-EDS mapping was collected to characterize elemental distribution and assess interfacial mixing. A range of magnifications was used to capture both the overall interfacial structure and the finer-scale solidification behavior across the diffusion zone.

2.6. Internal morphology and defects

Micro-computed tomography (CT) was performed on each specimen to evaluate the occurrence and distribution of as-built internal porous defects. Micro-CT was performed using the Phoenix v|tome|x L (Waygate Technologies, Germany) at a scanning voxel size of 15 µm. The Avizo software (version 2022.1, Amira-Avizo, FEI, Thermo Fisher Scientific, United States) was used to process the micro-CT volume files for digital analysis. Material sub-volumes were identified and segmented for material-wise analysis and visualization. Morphological analysis included relative pore density and spatial distribution, as well as part inspection for process-specific surface and internal process anomalies.

2.7. Multi-material computational fluid dynamics simulation

In this study, MM-PBF simulations were developed to understand the evolution of melt pools at and near the two material interfaces. The DEM using a Lagrangian framework was applied to simulate the deposition of a layer of powder. Multi-physics CFD modeling was applied to simulate melting using a Gaussian laser heat source in Flow3D AM software (version: 2025A, United States), using the volume-of-fluid method for tracking the phase interface and CFD to solve the thermo-fluid equations at each cell. The volume-of-fluid method calculates volume-averaged thermophysical properties of each cell, and conservation of energy, mass, momentum, and pressure was applied to solve for the computational domain.[40,41] For both material systems (316LSS and CuCrZr), temperature-dependent thermophysical properties presented in Table 5 were employed for the simulations. The heat source was enabled with angle-dependent Fresnel reflection with a maximum of 20 number of reflections. "Multi-material" physics model in Flow3D AM was used to model distinct materials in the same simulation setup. The properties of the fluid mixture in a single voxel were averaged to the volume fraction of fluids in the cell. The intermixing of two materials was solely dependent on the fluid dynamics of the two fluids in the computational domain, while molecular and turbulent diffusion caused by elemental dispersion were neglected in this study and will be a focus of future work.

Table 5. Material properties used for the computational fluid dynamics simulation study

Properties	Symbol	CuCrZr	316L	Unit
Density (@300 K)	ρ	8,930	7,954	kg/m^3
Specific heat (@300 K)	C_p	385	498.73	J/Kg/K
Thermal conductivity (@300 K)	K	400	13.96	W/m/K
Emissivity	ε	0.4	0.4	
Surface tension (@melting)	σ	1.304	1.7	kg/s^2
Absorptivity (Fresnel coefficient)	FC	0.2[42]	0.65[43]	

(*Cont'd...*)

Table 5. (*Continued*)

Properties	Symbol	CuCrZr	316L	Unit
Multiple reflection model with maximum number of reflections	-	20	20	
Saturation temperature (at atmospheric pressure)	T_{evap}	2835	3090	K
Accommodation coefficient for evaporation	AC_{evap}	0.01	0.01	
Accommodation coefficient for condensation	AC_{cond}	0.01	0.01	
Latent heat of vaporization	L_f	4.73×10^6	6.1×10^6	J/kg
Evaporation pressure coefficient	A		55728	
Evaporation pressure coefficient	B		9.48	
Liquidus temperature	$T_{liquidus}$	1,357.85	1,710	K
Solidus temperature	$T_{solidus}$	1,357.45	1,683	K

The simulation setup procedures for all five build orientations are presented in Figures 2 and 3. The procedure for orientations involving material change along the build directions (Figure 2) began by using DEM to deposit a powder layer of one material onto a substrate of the other, after which a moving laser scan is applied in the CFD model to capture the resulting melt pool and thermal-fluid behavior at the interfaces. For the vertical and diagonal interfaces (Figure 3), powders of two materials were settled adjacent to each other, and the substrate geometry was treated as the corresponding interface material. The simulation setup followed the same sequential scan sequence shown in Figure 1C to mirror the experimental scan sequence. CuCrZr powder was exposed first, and laser scans were simulated to approach the interface at 90°. FLOW-3D POST (version: 2025A, United States) was used for post-processing, analysis, and visualization of the simulation results.

3. Results

All five interface orientations were successfully fabricated as shown in Figure 1B. The as-built parts exhibited good dimensional resolution, and the interfaces between the two materials were visually distinct. Optical inspection did not reveal any large-scale delamination at the MM-LPBF interface or between the parts and the build plate. Wire electron discharge machining removed the microscopy coupons from the build plate, and the cubes were hot-mounted and polished for microstructural inspection (Section 3.1).

3.1. Scanning electron microscopy and energy-dispersive X-ray spectroscopy

Scanning electron microscopy and energy-dispersive X-ray spectroscopy analyses reveal that the microstructural evolution at the CuCrZr-316LSS interface in MM-LPBF is governed by a complex interaction between thermal transport, melt-pool dynamics, and the inherent immiscibility of copper and iron. When 316LSS is melted over CuCrZr, limited penetration of CuCrZr into the 316LSS layer is observed, which reduces the diffusion of CuCrZr into the 316LSS volume along the build direction (Figure 4A). Conversely, when CuCrZr is processed on the 316LSS layer, higher VED in the initial CuCrZr layers drives significant penetration into the 316LSS layer, producing an extended transition interface with substantial copper enrichment in the iron matrix (Figure 4C). This deeper CuCrZr penetration results in localized zones in the 316LSS that are susceptible to cracking, as observed across different interface orientations. Notably, the transition zone itself remains well-mixed and largely free of local defects, indicating that the metallurgical bonding in the interface is continuous despite the presence of cracks in the 316LSS volumes adjacent to the interface.

The horizontal interface of 316LSS deposited over CuCrZr exacerbates limited penetration due to the higher thermal conductivity of CuCrZr, which rapidly draws heat away from the 316LSS melt pool and restricts its progression beyond one to two re-melt layers. This is quantitatively demonstrated in the width of the interface shown in Figure 5. Laser scanning strategy and sequence of exposure are observed to greatly affect the interfacial mixing direction during laser melting and remelting. In the case of vertical interfaces, in which CuCrZr is exposed first, interfacial mixing favors CuCrZr powder transport into the unmelted 316LSS powder. Diagonal orientations produce an intermediate interface, combining the effects of both the vertical and horizontal interfaces.

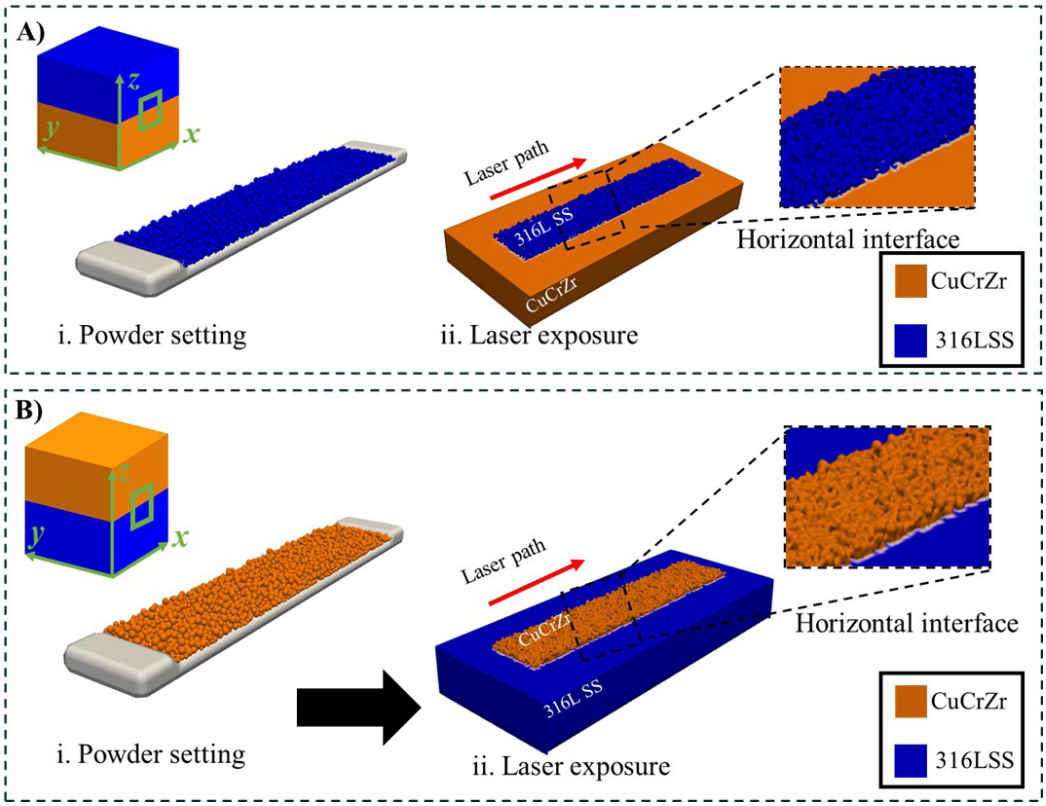


Figure 2. Computational fluid dynamics simulation setup procedure for orientations changing material along the build direction. (A) Discrete element method simulates the deposition of loose powder of a single composition across a simulated build plate. (B) The powder bed is applied over a finite bulk volume of the opposite material, and the laser path is applied across the powder bed.

Electron backscatter diffraction mapping demonstrated that the phase field and grain structure are influenced by the compositional and thermal asymmetries observed in Figure 4. Based on EBSD results presented in Figure 4, it can be observed that in MM-LPBF: (i) local phase insolubility is driven by rapid, compositionally heterogeneous solidification; and (ii) spatially varying nucleation and growth kinetics (equiaxed grain refinement vs. columnar growth) are controlled by localized cooling rates, solute content, and melt-pool hydrodynamics in determining layer bond quality when compared to single-material LPBF for either constituent material.[44,45]

Electron backscatter diffraction phase mapping in Figure 4 reveals body-centered cubic (BCC) (δ) grain formations embedded within the nominally austenitic 316LSS volume adjacent to the interface. A magnified view of local BCC grains in Figure 6 shows the phase-map morphology, and corresponding EDS maps indicate that these BCC pockets are correlated with local depletion of FCC-stabilizing elements (notably nickel and copper) and enrichment of BCC-stabilizing chromium. This is consistent with classical stainless-steel alloying phenomena: nickel is a strong austenite (FCC) stabilizer, and its local depletion promotes ferrite (BCC) formation, while chromium acts as a ferrite (BCC) stabilizer and its enrichment favors BCC phases. EBSD grain-boundary chemistry (EDS mapping localized to BCC island formation at high magnification in all orientations, Figure 6) shows decreased nickel and copper counts coincident with increased chromium counts in BCC-rich grains, supporting a composition-driven phase shift during rapid solidification. These conditions are specifically prominent in multi-material systems where element partitioning occurs during turbulent melt-pool mixing and rapid solidification.

3.2. Transmission electron microscopy

Transmission electron microscopy provides nanoscale observations of the phase and defect structures inferred from EBSD and XRD, though interpretation is inherently limited by the small scan area relative to the heterogeneous interface. Darker areas in the bright-field TEM images of Figure 7 indicate higher local dislocation density. EDS

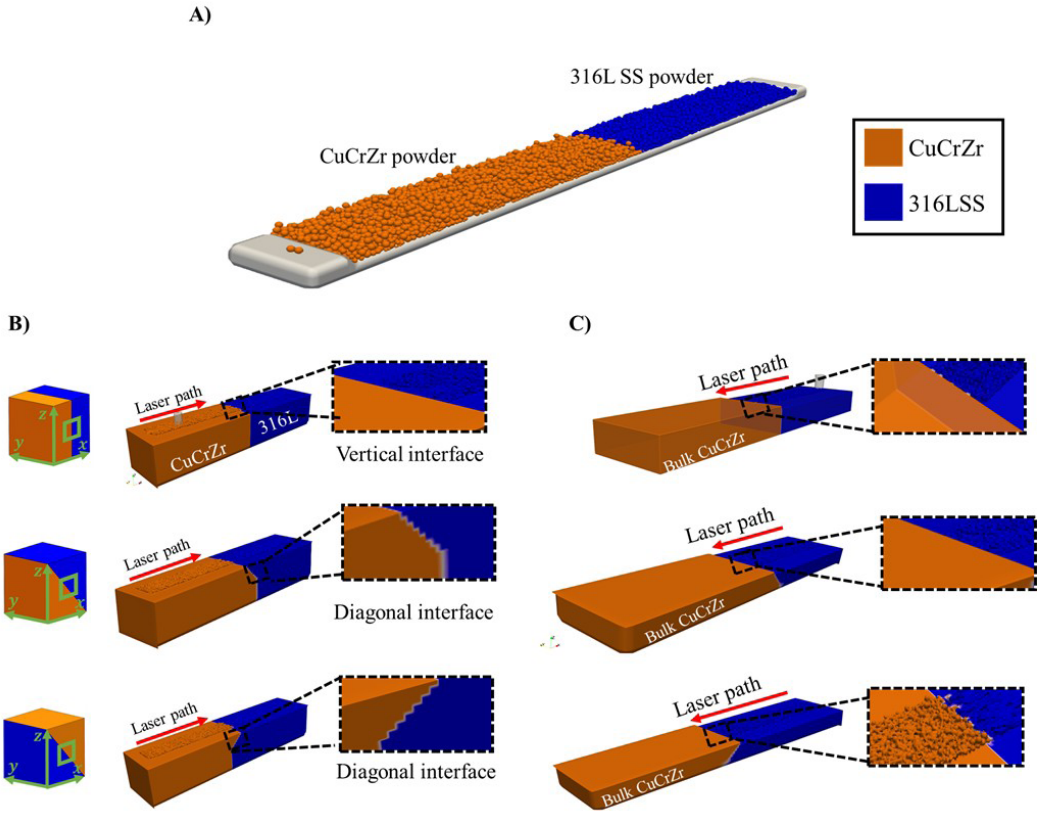


Figure 3. Computational fluid dynamics simulation setup procedure for intra-layer orientations, including the two diagonal interfaces and the straight vertical interface. (A) Discrete element method simulates the deposition of loose powder of two discrete compositions across a simulated build plate. (B) CuCrZr powder is exposed to a laser moving toward the vertical interface to the 316LSS powder. (C) 316LSS powder is exposed to a laser moving toward the vertical interface to the bulk CuCrZr volume.

scans provide elemental composition in these areas related to material- and orientation-specific dislocations. Figure 8 presents scans completed at the 100 nm scale. All interface orientations exhibit areas of partial dissolution, with islands of 316LSS inclusions within the CuCrZr grains and vice versa.

3.3. X-ray diffraction

X-ray diffraction was conducted to evaluate phase constitution and crystallite-scale structural variations across the CuCrZr–316LSS interface and is presented in Figure 9. Diffraction patterns did not reveal any unexpected phases beyond those corresponding to γ-austenite (FCC) and copper-rich (FCC) peaks, confirming the absence of significant intermetallic formation. A very low-intensity (110) reflection characteristic of BCC δ-ferrite was observed consistently across all orientations, supporting the EBSD evidence for localized ferrite formation near the interface. The limited intensity of this peak indicates that ferrite volume fraction remains low, consistent with the narrow BCC bands observed in the EBSD phase maps. The average crystallite size, obtained from peak broadening analysis using the Scherrer equation, varied with build orientation. It is important to note that a smaller calculated crystallite size in this context reflects an increase in the number of fine crystallites within the analyzed sample volume, and not necessarily a uniform reduction of all grain sizes.

3.4. Micro-computed tomography

Micro-CT scans of the microscopy cubes are presented in Figure 10. The reconstructed volumes display the internal defect distribution for each orientation in both isotropic and orthogonal views, allowing visualization of defect morphology and spatial trends throughout the volumes. Quantitative defect values were extracted for each material zone, and the material-wise defect densities are reported as a percentage of the total volume for their respective material sub-volumes. Across the orientations, a patterned distribution of defects was observed, as indicated by

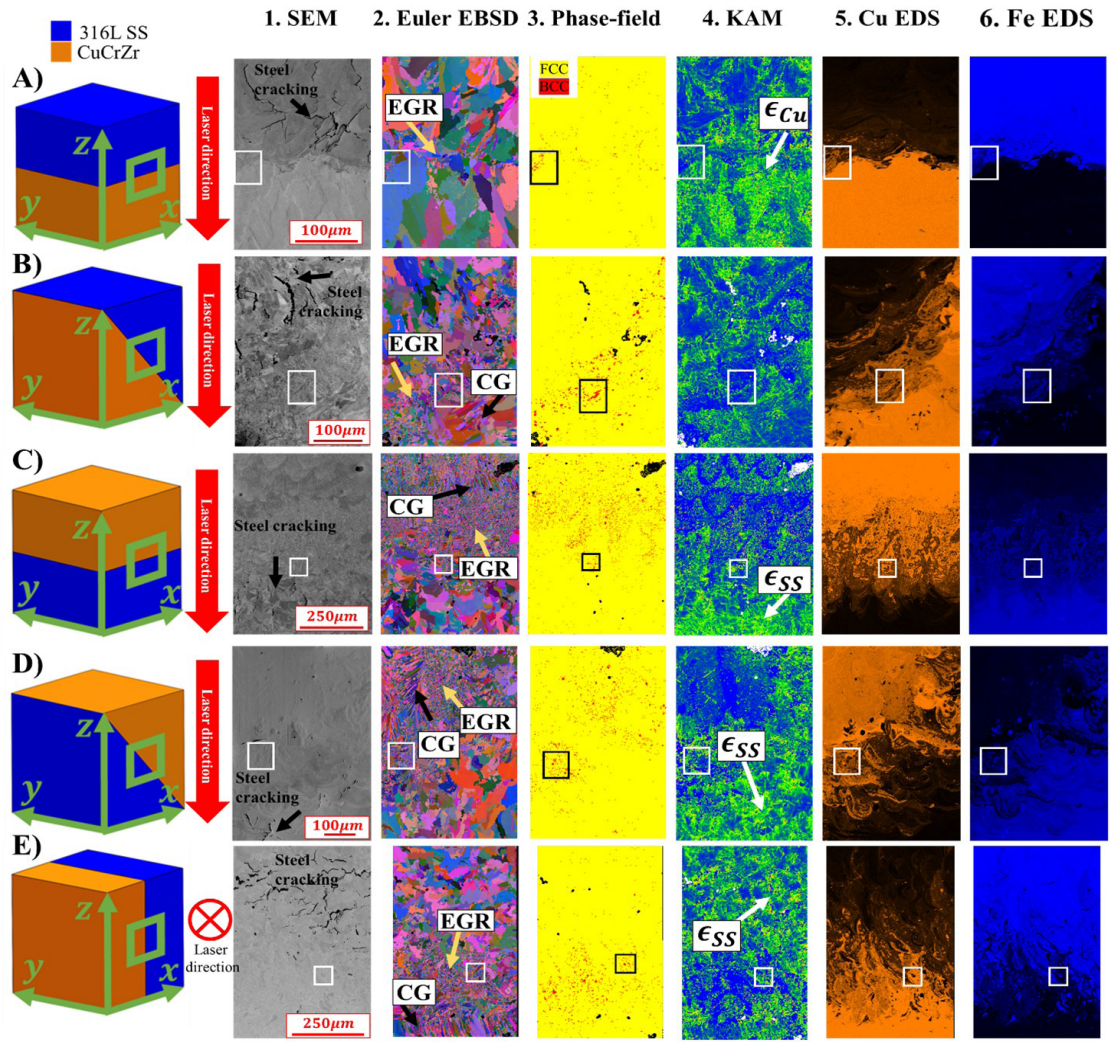


Figure 4. SEM, EBSD, and EDS images from 316LSS-CuCrZr direction-dependent witness cubes in a wide-field view showing the full interface. Euler EBSD identifies equiaxed grain refinement (EGR) at the interface and columnar grain (CG) growth within the CuCrZr. KAM maps present high strain in either the CuCrZr ($\in_{Cu}$) or 316LSS ($\in_{SS}$). Boxed areas of interest correspond to the high-resolution scans presented in Figure 6. (A) SS316L over CuCrZr, (B) CuCrZr\SS316L, (C) CuCrZr over SS316L, (D) SS316\CuCrZr, (E) Adjacent. Scale bars: 100 μm, 250 μm; magnifications: 600×–1,300×. Abbreviations: EBSD: Electron backscatter diffraction; EDS: Energy-dispersive X-ray spectroscopy; SEM: Scanning electron microscopy.

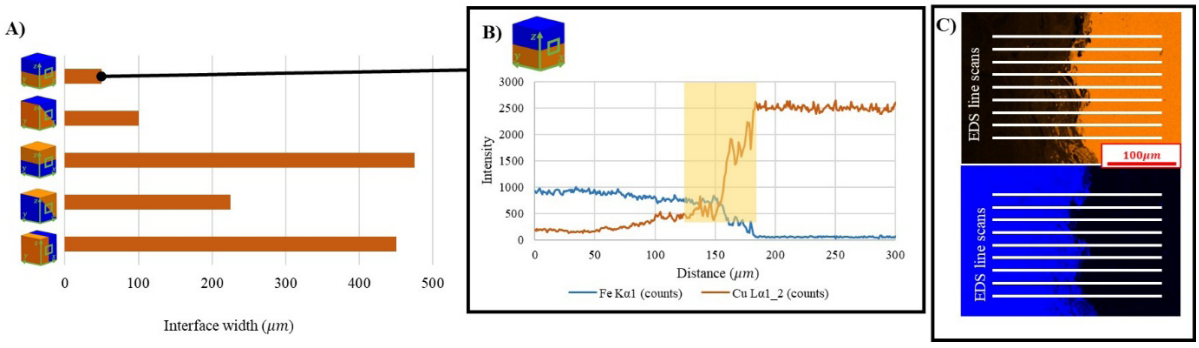


Figure 5. Width of the interface for 316LSS and CuCrZr microscopy coupons, according to energy-dispersive X-ray spectroscopy (EDS) line scan data. (A) Width of the interfacial region of 316L stainless steel and CuCrZr, according to the multi-material laser powder bed fusion build orientation. (B) Averaged EDS line scan intensity for 316L stainless steel printed over CuCrZr. (C) EDS line scans. Scale bar: 100 μm.

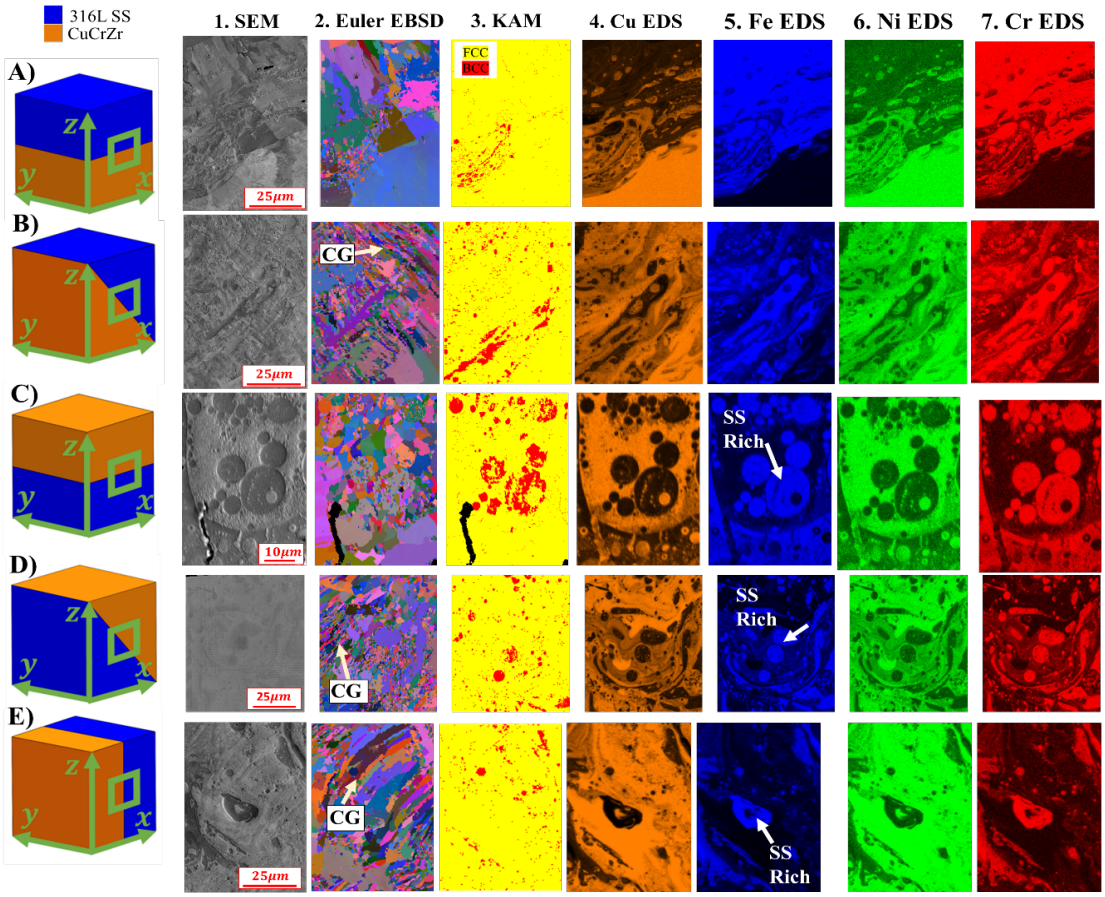


Figure 6. SEM, EBSD, and EDS images from 316LSS-CuCrZr direction-dependent witness cubes in a high-resolution scan taken from a well-mixed area of interest, determined in Figure 4. (A) SS316L over CuCrZr, (B) CuCrZr\SS316L, (C) CuCrZr over SS316L, (D) SS316\CuCrZr, (E) Adjacent. Scale bars: 10 μm, 25 μm; magnifications: 600×–1,300×.
Abbreviations: EBSD: Electron backscatter diffraction; EDS: Energy-dispersive X-ray spectroscopy; SEM: Scanning electron microscopy.

black arrows in Figure 10. The pore distribution tended to accumulate near the material interface. This interfacial clustering again suggests that the multi-material transition zone may be a dominant source of process-induced defect formation, potentially driven by mismatches in thermal properties and melt-pool dynamics.

Quantitative defect analysis further reveals that CuCrZr consistently exhibits higher defect densities than 316LSS. The average relative density of the CuCrZr volume was 99.70%, whereas the 316LSS volume achieved a higher density of 99.97%. This trend aligns with known challenges in single-material LPBF processing of CuCrZr and is attributed to the inherent difficulty in processing copper due to its higher reflectivity and thermal conductivity, as reported in prior studies.[46,47] These material properties reduce energy absorption and increase heat dissipation, respectively, thereby decreasing melt-pool stability and promoting pore formation.

3.5. Nanoindentation

Figure 11 presents the nanoindentation results obtained from bulk volumes of CuCrZr and 316LSS, as well as from the well-mixed interfacial area. Quantitatively, CuCrZr volume across all orientations showed hardness values between 1.44 and 1.73 GPa, whereas 316LSS volume exhibited values ranging from 3.25 to 3.57 GPa. The interfacial area displayed intermediate hardness values, ranging from 2.49 to 2.97 GPa, indicating a gradation of mechanical properties across the interface.

The hardness of bulk CuCrZr produced via single-material LPBF has been reported in the literature to range from 1.28 GPa (130 HV) to 1.88 GPa (192 HV).[48,49]

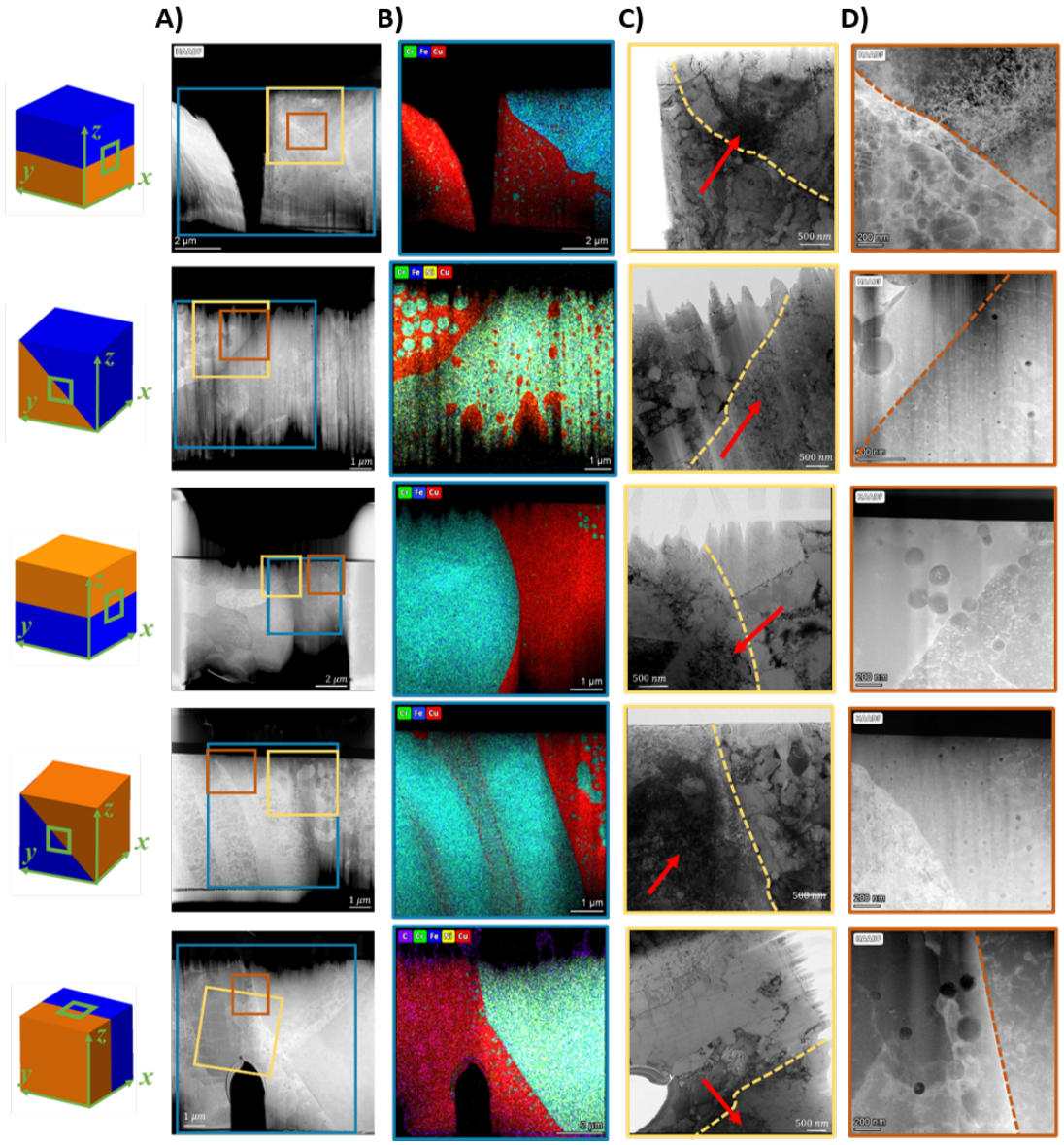


Figure 7. STEM and EDS images from 316LSS-CuCrZr direction-dependent witness cubes. Focused ion beam samples were extracted from a well-mixed interfacial area of each cube. TEM wide-field column shows a 1–2 µm-scale scanned image. Colored boxes of interest correspond to the colored outline images in the following columns. Red arrows present areas of high dislocation density within the 316LSS. Dotted lines follow a grain boundary joining dissimilar materials. (A) TEM: Wide-field. (B) EDS: Wide-field. (C) TEM: High-angle annular bright-field. (D) STEM: High-angle annular dark-field. Scale bars: 1 µm, 2 µm, 200 nm, 500 nm; magnifications: 600×–1,300×.
Abbreviations: EDS: Energy-dispersive X-ray spectroscopy; STEM: Scanning transmission electron microscopy.

The measured hardness values at locations adjacent to the interface within the CuCrZr volume are within this expected range. Similarly, printed 316LSS has been reported to exhibit hardness values from 1.92 GPa[50] to 3.68 GPa,[51] consistent with the measurements observed in the present study. These results demonstrate that the interfacial hardness is consistently between that of the two constituent materials, while the hardness of the individual materials agrees with expected bulk LPBF properties.

Young's modulus was determined at all locations using the Oliver and Pharr method. Consistent with the hardness trends, the modulus of the interfacial area was found to be intermediate relative to the parent materials, further confirming the mechanical gradation across the interface.

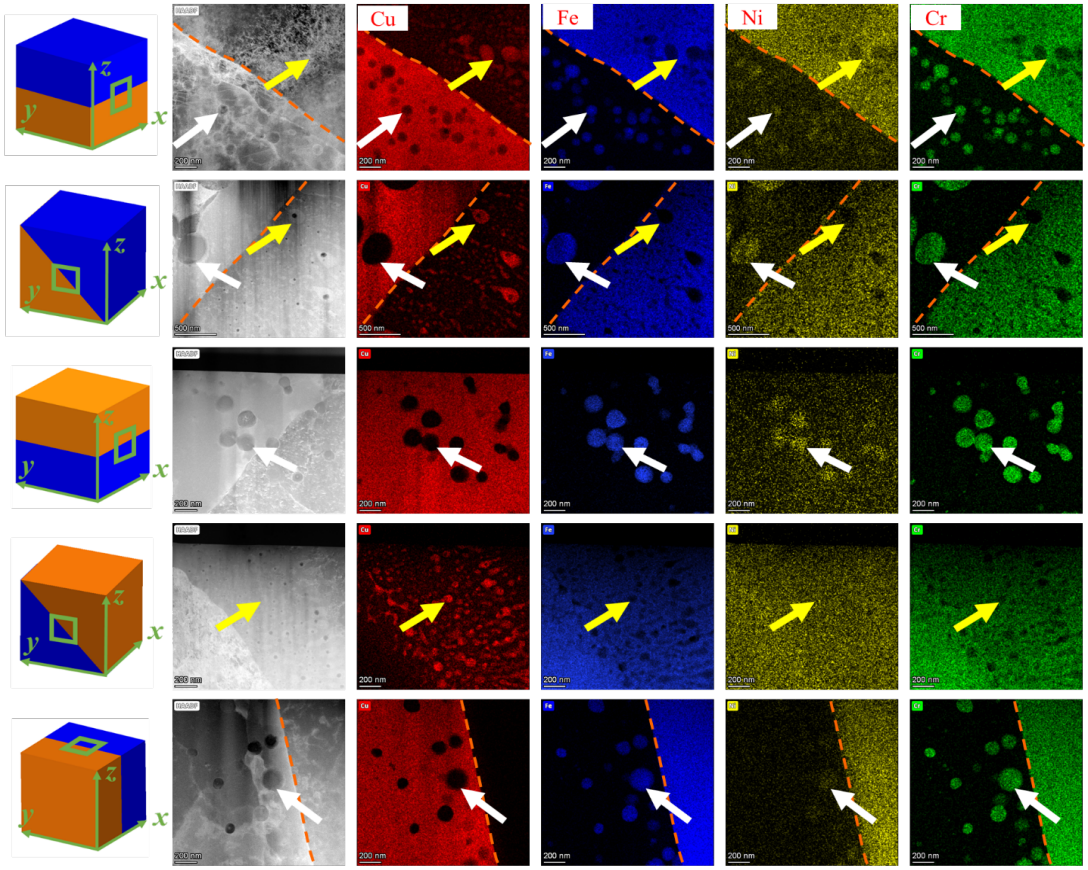
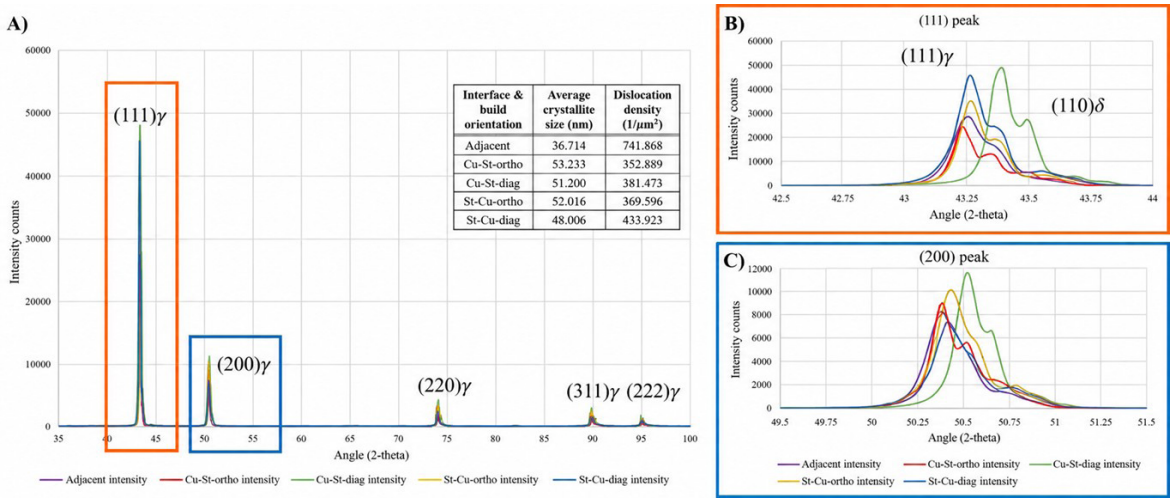


Figure 8. STEM images from 316LSS-CuCrZr direction-dependent witness cubes with EDS for copper (Cu), iron (Fe), nickel (Ni), and chromium (Cr) composition. Focused ion beam samples were extracted from well-mixed interfacial areas of each cube. White arrows indicate 316LSS inclusions within the CuCrZr, and yellow arrows indicate CuCrZr inclusions within the 316LSS. Orange dotted lines follow a grain boundary joining dissimilar materials. Scale bars: 1 µm, 2 µm, 200 nm, 500 nm; magnifications: 600×–1,300×.
Abbreviations: EDS: Energy-dispersive X-ray spectroscopy; STEM: Scanning transmission electron microscopy.



Interface & build orientation	Average crystallite size (nm)	Dislocation density (1/µm²)
Adjacent	36.714	741.868
Cu-St-ortho	53.233	352.889
Cu-St-diag	51.200	381.473
St-Cu-ortho	52.016	369.596
St-Cu-diag	48.006	433.923

Figure 9. X-ray diffraction from 316LSS-CuCrZr direction-dependent witness cubes. Average crystallite size (nm) and dislocation density calculated according to the Scherrer method. X-ray diffraction measurements were taken using an approximate beam area of 2.5 mm × 5 mm across the interfacial area. (A) Whole X-ray diffraction diffractogram. (B) Zoomed (111) peak. (C) Zoomed (200) peak

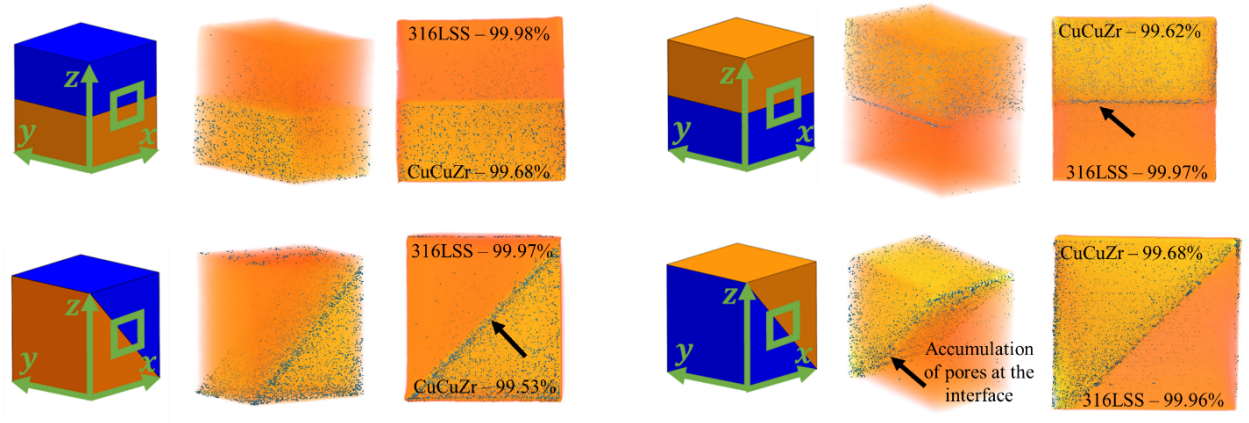


Figure 10. Micro-computed tomography results depicting the internal defect distribution (likely pores) of microscopy coupons. Materials are labeled on each orientation, denoting orange as 316LSS and yellow as CuCrZr. Dark areas depict internal defect volume along with material-wise volumetric density.

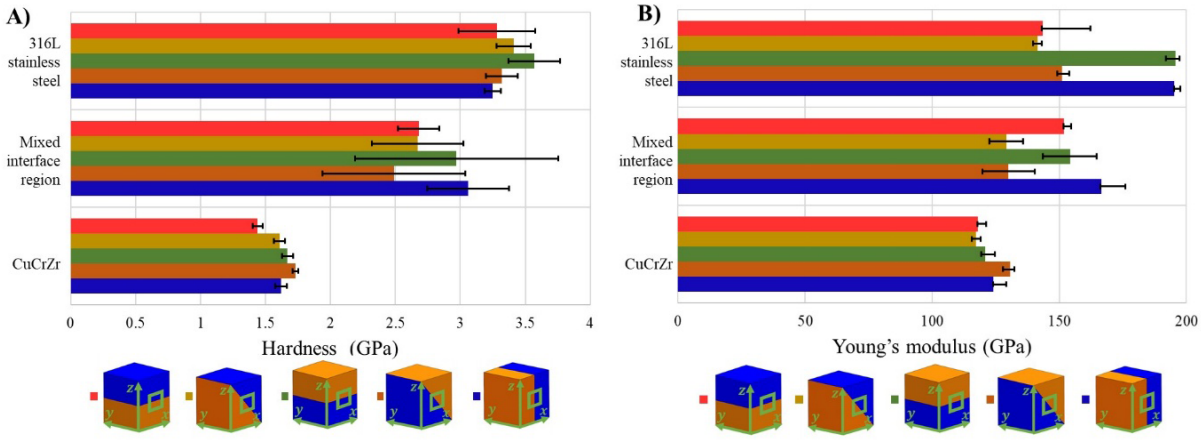


Figure 11. Nanoindentation results for CuCrZr, 316LSS, and the interfacial area showing orientation-dependent (A) hardness and (B) Young's modulus calculated using the Oliver and Pharr method. Measurements were taken from single-material volumes and the well-mixed interface, with a minimum of three random representative indents per location. Error bars represent the mean ± one standard deviation

3.6. Computational fluid dynamics mixing simulation

The CFD-predicted temperature distribution and melt-pool morphology for all five interface orientations under single-track laser exposure are summarized in Figures 12 and 13, respectively. For each orientation, the melt-pool depth, width, and transient melt-pool evolution both at the interface and in the bulk material of each alloy were analyzed. These parameters are directly tied to the prediction of melt-pool stability, energy absorption, convective flow behavior, and the severity of material mixing. Importantly, the CFD predictions capture how the extreme thermal conductivity mismatch between CuCrZr and 316LSS, coupled with different absorptivity values and latent heat, influences melt-pool asymmetry and penetration depth. The vertical and diagonal orientations include a combination of two simulation cases each, with the laser approaching the vertical interface from either the CuCrZr or 316LSS volumes, allowing direct comparison of directional effects on keyholing, dilution, and defect formation as the laser approaches the other bulk material section.

In the horizontal interface orientation, the CuCrZr over 316LSS track exhibits an unstable melt pool with deeper melt pool penetration ranging from 180–200 μm, as seen in Figure 13A. This instability arises because the

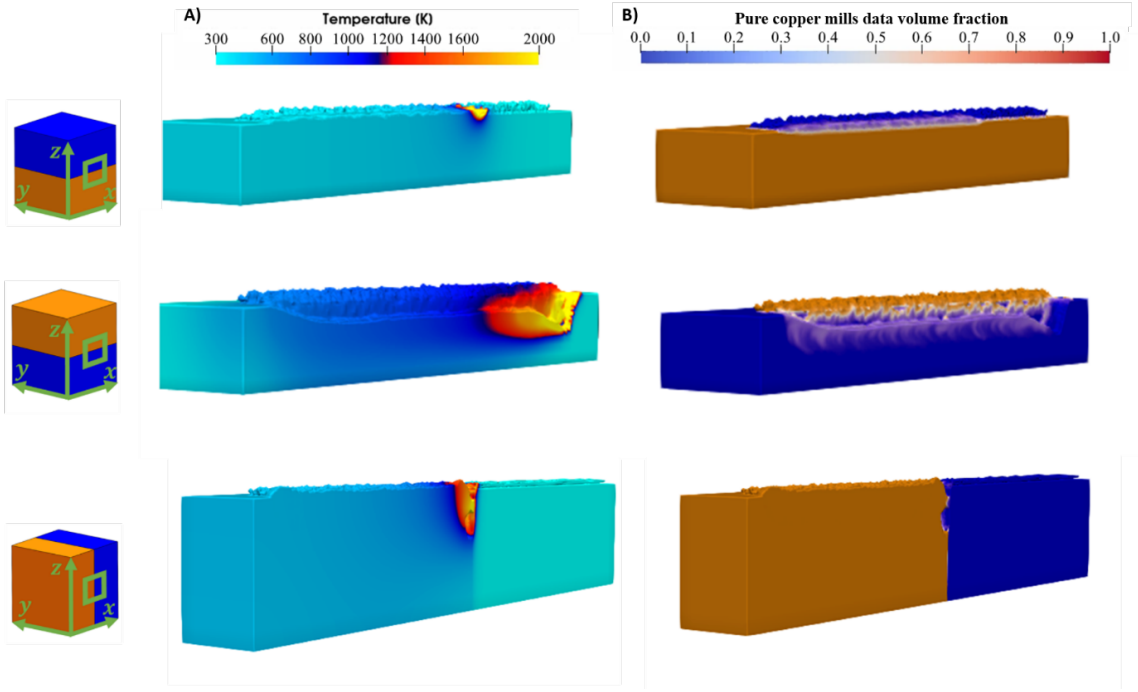


Figure 12. Computational fluid dynamics-predicted temperature distribution and melt-pool morphology for all five interface orientations under single-track laser exposure. (A) Computational fluid dynamics temperature distribution mid-laser track. (B) Percent copper fraction for orthogonally oriented build directions.

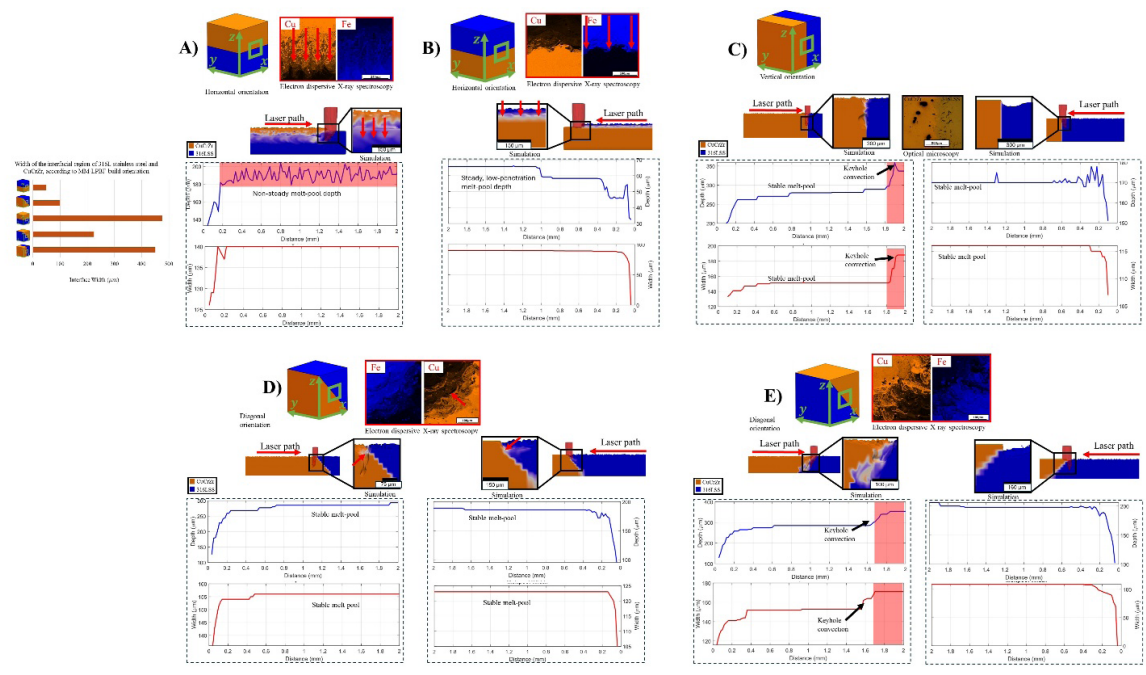


Figure 13. Melt-pool depth and width for the five fundamental building orientations with simulation for (A) CuCrZr melted over 316LSS across a horizontal interface, (B) 316LSS melted over CuCrZr across a horizontal interface, (C) both materials printed across a vertical interface, (D) CuCrZr over 316LSS diagonally, (E) 316LSS over CuCrZr diagonally. Orientations (C–E) include the laser path approaching the interface from both bulk material volumes. Scale bars: 75 μm, 150 μm; magnifications: 600×–1,300×.

first CuCrZr layer is processed with high-VED CuCrZr material parameters, yet the underlying substrate contains substantial 316LSS, which is remixed within the melt pool. This effect is observed to be the most severe in the first layer transition from 316LSS to CuCrZr along the build direction. The lower thermal conductivity of 316LSS relative to CuCrZr hinders heat extraction, promoting keyhole-mode penetration and vigorous Marangoni convection. Conversely, the 316LSS over CuCrZr track shows a shallower, more stable melt pool with penetration around 65 μm (Figure 13B), as the higher-conductivity CuCrZr substrate rapidly dissipates heat, shortening the liquid lifetime and suppressing melt-pool instabilities. These observations highlight the directional dependence of energy dissipation and interactions between the thermal properties of multi-material systems and AM processing conditions (e.g., laser power and scan speed) that influence the melt-pool morphology.

For the vertical interface orientation, where the material boundary is perpendicular to the build plate (Figure 13C), the CFD simulations show strong defect formation dependence with respect to both the build direction and the direction of the laser approaching the interface. As the laser approached the vertical interface from the CuCrZr, the melt pool remained stable until approximately 200 μm from the 316LSS volume, at which point convective instability occurs. This results in relatively higher melt-pool depth and width, indicative of unstable Marangoni flow and pore formation near the interface. In contrast, the laser approaching the vertical interface from the 316LSS produces a more stable melt pool with relatively minimal depth fluctuation, reflecting efficient heat extraction by CuCrZr and suppression of keyhole formation. These trends demonstrate that the relative position of the laser with respect to the thermal conductivity gradient strongly affects both the melt-pool behavior and the localized interfacial mixing.

Diagonal orientations (Figure 13D & 13E) introduce simultaneous vertical and lateral composition changes during scanning, producing melt-pool mixing that blends characteristics of both the horizontal and vertical interface cases. The simulations indicate stable melt pools, although the horizontal interface melting CuCrZr into 316LSS shows a moderate increase in melt-pool depth within 300 μm of the interface. This localized deeper melt pool suggests partial keyhole convection as the melt pool begins to intersect 316LSS-rich volumes, which likely resulted in slower heat removal and increased energy absorption. Although this observed phenomenon was less severe than the vertical interface case, it is consistent with the same underlying principle that the laser parameters optimized for higher conductive CuCrZr generate a disproportionately energy-dense melt pool when the underlying substrate locally exhibits 316LSS-rich thermal properties. These results are consistent with the observations made in the micro-CT analysis; a higher concentration of defects is observed in the CuCrZr volume closer to the interface.

Across all orientations, the CFD simulations reveal that melt-pool stability and penetration are strongly influenced by the interactions between laser processing regimes, thermal conductivity contrasts, and interface orientations. Areas of increased melt-pool depth and convective instability correspond to locations where Marangoni-driven flows are enhanced by steep local temperature gradients, whereas shallow, stable melt pools occur where higher conductive substrates or prior layers promote rapid heat removal. The simulations provide new insights into the relative severity of interfacial mixing and highlight the influence of directional laser approach on localized fluid dynamics.

4. Discussion

4.1. Solidification-based defects and behavior

At the microscale, SEM and EDS observations indicate that the immiscibility of copper and iron drives the formation of discrete copper-rich and iron-rich liquid domains within the solidification front.[52] This is consistent across all orientations, as evidenced in the high-magnification EDS of Figure 6. Evidence of liquid metal embrittlement (LME) is observed in the 316LSS volume near cracking sites[53] across all interface orientations at varied degrees of severity (presented in labeled SEM images of Figure 4). This is a result of copper-rich liquid wetting and penetration into 316LSS grain boundaries or weakened inter-dendritic regions during thermal excursions, reducing intergranular strength during solidification and promoting crack initiation under thermomechanical-induced stresses or solidification strain. This type of defect is a result of both material incompatibility and process-induced conditions which inhibit or promote copper mixing into the bulk 316LSS volume. Solidification cracking was most prevalent when CuCrZr and 316LSS were printed within the same layer at a vertical interface (Figure 4E), correlating with one of the more elongated interfaces (Figure 5) containing a higher degree of CuCrZr contamination in 316LSS. Several experimental and review articles report similar LME behavior and attribute cracking to copper wetting of iron boundaries and to the presence of segregated copper-rich liquid during rapid solidification.[2,31,54]

Micro-CT in Figure 10 reveals that defects frequently occur deep within the 316LSS when CuCrZr is deposited

over 316LSS at high VED, indicative of convection-dominated melt-pool instability. Marangoni-driven convective fluid flow promotes intensive turbulent mixing at the boundary, intensifying the relative mixing and local redistribution of elements across the transition zone.[2,55] Despite this mixing, the inherent immiscibility between copper and iron limited the extent of solid-solution formation. As a result, the interface exhibits distinct copper-rich and iron-rich domains (Figure 4), consistent with the well-documented copper–iron miscibility gap.[56–58] The turbulence induced by this Marangoni flow promotes local mixing and interfacial continuity, but the thermodynamic tendency for phase separation results in the persistence of compositionally distinct islands. Under LPBF's extreme cooling rates (ranging from $10^5 - 10^7 \frac{K}{s}$)[59] and higher thermal gradients provided by this extreme material pairing, any incipient liquid–liquid phase separation or solute-rich/solute-poor liquid region that form can be trapped by rapid solidification, producing fine copper- or iron- enriched features (e.g., droplets, scattered fragments) within the solidified matrix. Rapid convective mixing can disperse these copper-rich liquid fragments throughout the melt pool at a macro-scale, and within individual grains at a micro-scale. Upon solidification, these fragments act as embrittling phases or potential stress concentrators under mechanical load.[60] The high-resolution EDS maps suggest that these islands remain independent, with no evidence of micron-scale intermetallic compound formation, consistent with prior studies of 316LSS and CuCrZr systems.[61–63]

4.2. Microstructure and phase composition

Grain-size and shape analysis from EBSD maps (Figure 4, column 2) confirm that 316LSS grains in closer proximity to the interface are larger than CuCrZr grains. This observation aligns with single-material LPBF and conventional microstructure data, which show that additively manufactured 316L typically exhibits cellular and columnar austenitic grains in the order of several to a few tens of micrometers, depending on scan strategy and thermal history,[64,65] whereas CuCrZr often solidifies with finer cells and shorter columnar grain lengths due to its narrower mushy zone and higher nucleation undercooling.[49] Mechanistically, the smaller mushy zone in CuCrZr, due to the narrower temperature interval between liquidus and solidus for the effective alloy composition and precipitate-stabilized microstructure, results in limited time for dendrite coarsening and reduces grain growth during solidification.[66,67] The rapid solidification associated with LPBF processing further traps finer microstructural features.[68] Where columnar CuCrZr grains are observed, they align with directions of sustained thermal gradient and directional solidification during re-melting events, consistent with epitaxial columnar growth under steep G/R (thermal gradient to grain growth rate) conditions.[47,49] This phenomenon is particularly evident in the columnar grain growth labeled on the EBSD images of Figure 4B, C, D, & E).

Electron backscatter diffraction Euler orientation-map analyses indicate a pronounced area of grain refinement centered in the EDS-identified mixed zone. Regions of equiaxed grain refinement at the mixed interface are labeled in the EBSD of Figure 4. The width of this EBSD-refined band matches the EDS-identified mixed zone, suggesting that turbulent melt pool mixing and increased local nucleation density during solidification produced a refined, equiaxed microstructure at the chemical transition that characterizes the interfacial area. The mixed melt pool contains numerous compositionally distinct liquid fragments and thermal heterogeneities that act as distributed nucleation sites as the melt undercools. Figure 6 shows higher magnification of EBSD and EDS sub-volumes identified by boxes in Figure 4. The combined effect of high nucleation density and rapid solidification kinetics produces equiaxed grains and strong local refinement. In the horizontal interface case of 316LSS deposited over CuCrZr, the EBSD shows only a minimal refinement band (the mixed zone is narrow, evident in Figure 4A & 6A), whereas the vertical, diagonal, and horizontal cases of CuCrZr deposited over 316LSS build much wider refinement zones (Figure 4C). This is quantifiably evident by the EDS line scans (Figure 5) across all interfaces, which reveal an interfacial width of 50 μm versus 475 μm for these two orientations. Qualitatively, this observation is also aligned with EDS evidence presented in Figure 4, which shows that the horizontal interface depositing CuCrZr over 316LSS generates more extensive CuCrZr entrainment and turbulent mixing.

The localized formation of BCC ferrite within the 316LSS contributes to localized microstructural and mechanical heterogeneity near the interface. The BCC ferrite formation is presented for all orientations in Figure 4, and in the higher-magnification sub-volumes of Figure 6. Literature on austenite-ferrite boundaries has reported that chemical segregation of elements is partially controlled by interfacial crystallography, with chromium enrichment and copper depletion in ferrite grains.[69–71] Localized element segregation is most evident in Figure 6C, where spherical BCC grains of chromium and iron enrichment, and copper and nickel depletion occur; however, this is prevalent across all orientations shown in Figure 6. This partitioning leaves copper-enriched inter-dendritic films or residual liquid films in the immediate vicinity of the local austenite matrix. Such compositional heterogeneity

increases susceptibility to LME, as copper-rich films at austenite boundaries can serve as diffusion paths and crack initiation sites under strain.[72] Furthermore, other studies have shown that ferrite possesses a higher modulus and lower ductility than the surrounding austenite,[73] and its presence introduces strain mismatches[74] that concentrate thermal and mechanical stresses during layer deposition and cooling. The thermal history unique to processing CuCrZr and 316LSS simultaneously reinforces this ferritic solidification behavior.

In short, when 316LSS is deposited with CuCrZr across a vertical interface, or deposited and exposed above CuCrZr across a horizontal interface, the steep thermal gradients imposed by the CuCrZr substrate increase the local temperature gradient. The resulting high gradient but moderate solidification rate conditions favor ferrite solidification,[75] as ferrite is stable at higher temperatures subject to rapid cooling.

Kernel average misorientation analysis reveals that patterned local strain distributions at the CuCrZr-316LSS interface are strongly dependent on build orientation. In the horizontal interface orientation depositing 316LSS over CuCrZr, high KAM values are observed within the CuCrZr layer (Figure 4A), indicating that this is the only interface orientation in which the CuCrZr experiences significant strain. Notably, in the vertical interface orientation (Figure 4E) or the horizontal and diagonal interface orientations (Figure 4C, 4D), the 316L-SS layer exhibits higher internal strain, as supported by prior thermomechanical simulations in similar iron–copper material systems.[3] These observations indicate that both the sequence of material deposition and the scan strategy play a critical role in determining the location and magnitude of residual strain, which can influence local mechanical behavior and potential sites for crack initiation.

4.3. Strain dislocation and intragranular segregation

High-resolution TEM reveals isolated volumes of elevated dislocation density within the 316LSS matrix, visible as dark contrast lines corresponding to lattice distortions as shown in Figure 7. These defects are often attributed to mismatch in CTE (unlikely in this study) and rapid solidification shrinkage stresses, particularly in 316LSS grains constrained by already-solidified CuCrZr volume when layering along the build direction. Such localized strain accumulation is characteristic of LPBF-fabricated heterogeneous metals and has been widely reported in iron–copper systems where constrained solidification generates thermomechanically induced stress concentrations at the material boundaries.[3] In reported literature, similar dislocation-dense areas have been linked to dislocation entanglement under rapid solidification and subsequent thermal cycling.[76] These substructures act as potential nucleation sites for secondary precipitates, as reported in other high-cooling-rate LPBF alloys such as aluminum–scandium–zirconium systems,[77] though in the present iron–copper system, the diffusion distances and solubility limits make such secondary precipitation unlikely.

Figure 8 shows intragranular heterogeneity because of 316LSS and CuCrZr inclusions within mutual grains. Localized in volumes adjacent to the grain boundary, the TEM presents evidence of 316LSS inclusions within the CuCrZr grains, and vice versa. The composition of these areas observed by the STEM and EDS images in Figure 8 suggest that these are retained 316LSS or Cu-rich inclusions rather than intermetallic compounds, consistent with the XRD results that showed no unexpected phase peaks. Given the immiscibility of iron and copper and rapid solidification conditions, this morphology may be attributed to incomplete diffusion and phase segregation during the final stages of cooling. The TEM findings reinforce a microstructural display of non-equilibrium segregation governed by steep thermal gradients, constrained solidification, and elemental immiscibility.

From a mechanical performance perspective, the presence of high dislocation densities can partially account for a discrepancy between simulated and experimentally measured yield strengths in LPBF-processed samples.[78] Idealized crystal plasticity simulations typically assume defect-free lattices, whereas real microstructures contain dislocation networks that serve as both strengthening and embrittlement sites depending on density and spatial distribution. TEM provides experimental validation for such defect structures. These dislocations manifest as dark lines in bright-field imaging due to localized electron diffraction contrast, and their relative density is proportional to the extent of plastic strain or residual stress.[78,79]

4.4. Crystalline structure from X-ray diffraction

X-ray diffraction provides further insights into the crystalline structure, chemical composition, and physical properties across the interface. Figure 9 presents the XRD intensity for all five interface orientation-dependent cubes, combined with the average crystallite size and size-derived dislocation density estimated across the interface using the Scherrer equation. Both 316LSS and CuCrZr are known to be present as FCC under nominal processing conditions. The formation of $(110)\,\delta$ peak adjacent to the $(111)\,\gamma$ peak provides evidence of the formation of BCC in minor quantities within the FCC multi-material matrix, further supported more directly by EBSD data at two scales in both Figures 4 and 6.

Smaller crystallite size and broader diffraction peaks collectively indicate higher dislocation density estimates,[80,81] reflecting an accumulation of lattice defects and stored strain energy during rapid solidification. As the FWHM of diffraction peaks increases, the corresponding peak intensity decreases, a relationship often associated with partial dynamic recrystallization under high cooling rates,[82] which is particularly relevant to this material pairing. The vertical interface orientation, which exhibits more intensive, turbulent mixing and grain refinement, according to the EBSD presented in Figure 4E. This orientation also presents the smallest average crystallite size as determined by the Scherrer method (Figure 9). This trend is consistent with the microstructural evidence of highly refined grains at the interface (Figure 4E). High dislocation density and fine crystallite structures increase local strength through dislocation–grain boundary interactions (Hall–Petch strengthening[83]) but carry some further implications on the material's susceptibility to environmental degradation mechanisms. In stainless steels, the elevated defect density increases the likelihood of hydrogen trapping within the lattice along dislocation cores and raises the potential for hydrogen-assisted cracking or embrittlement.[79] This interpretation may be particularly relevant in localized BCC formation, as this crystallite structure has been shown to be more susceptible to hydrogen embrittlement than a purely austenitic 316LSS.[79]

4.5. Predictive computational fluid dynamics melt-pool simulation

The CFD results demonstrate that thermal conductivity, absorptivity mismatch, and laser-material interaction are the primary determinants of melt-pool dynamics in MM-LPBF of extreme material interfaces. Deep, unstable melt pools in the CuCrZr over 316LSS horizontal interface orientation arise because the first CuCrZr layer is processed with higher-VED CuCrZr processing conditions, yet the underlying substrate contains substantial 316LSS, which is remixed within the melt pool. This effect is the most severe in the first layer transition from 316LSS to CuCrZr along the build direction. The lower thermal conductivity of 316LSS (13.96 $\frac{W}{mK}$ [84]) relative to CuCrZr (~400 $\frac{W}{mK}$ [45]) hinders heat extraction, promoting keyhole-mode penetration (Figure 13A) and vigorous Marangoni convection. EDS analysis of the interface in this orientation (Figures 4C & 13A) show an elongated interface with a severe penetration depth. In contrast, the reverse sequence of 316LSS over CuCrZr exhibits shallower but more stable melt pools (Figure 13B), reflecting rapid heat dissipation into the CuCrZr substrate. This effect will become less severe as more 316LSS layers are built along the build.

These trends reflect the experimental interfacial widths measured from EDS line scans in Figure 5, where the CuCrZr over 316LSS horizontal interface exhibits a total diffusion/mixing width of ~475 μm, while the 316LSS over CuCrZr horizontal interface remains narrow at ~50 μm, attributed to the VED difference. The CFD simulations of a single track can provide melt-pool tail lengths that cannot be easily quantified from experimental data of bulk samples. The simulated tail lengths (see comparison for the CuCrZr over 316LSS and 316LSS over CuCrZr horizontal interface orientations in Figure 12) follow the same trend and are governed by differences in thermal conductivity and specific heat capacity. Marangoni convection is expected to be strongly influenced by the melt-pool tail length, as a longer tail increases the available molten volume and residence time.

Vertical interface orientations further highlight the role of interfacial thermal gradients and extreme differences in melt properties. When the laser approaches the 316LSS interface from the CuCrZr, the melt pool remains stable until 200 μm from the interfacial plane, where the simulation predicts the onset of convection-driven instability (Figure 13C). Both melt-pool depth and width increase abruptly as the material composition seen by the top of the laser transitions from CuCrZr to 316LSS. The injection of 316LSS into the front upmost portion of the keyhole (Figure 14B) dynamically changes the local velocity (Figure 14C) and viscosity (Figure 14D) of the melt pool and can lead to keyhole collapse. In this regime, pore formation occurs at the boundary because the viscosity of the injected 316LSS is insufficient to support effective backflow into the keyhole, preventing pore closure. It can be observed from Figure 14 that, at the instance prior to keyhole collapse, 316LSS (denoted by white arrows) is injected into the top of the melt pool and causes a local drop in velocity and a spike in viscosity. Experimentally, defects (likely pores) of similar size, shape, and location are visible in the optical microscopy images, indicating that the CFD model accurately captures the melt-pool instability response at the interface.

Conversely, when the laser approaches the interface from 316L, the simulation predicts a fully stable melt pool (Figure 13C) with no keyhole-driven porosity. The optical images confirm the absence of pores but show areas of interfacial cracking instead. These cracks originate from solidification incompatibility and the iron–copper miscibility gap rather than melt-pool dynamics and therefore lie outside the predictive capability of mesoscale thermal-fluid simulations. Nonetheless, the CFD captures the underlying reason for process-induced defect formation; as the melt-pool transitions from low-

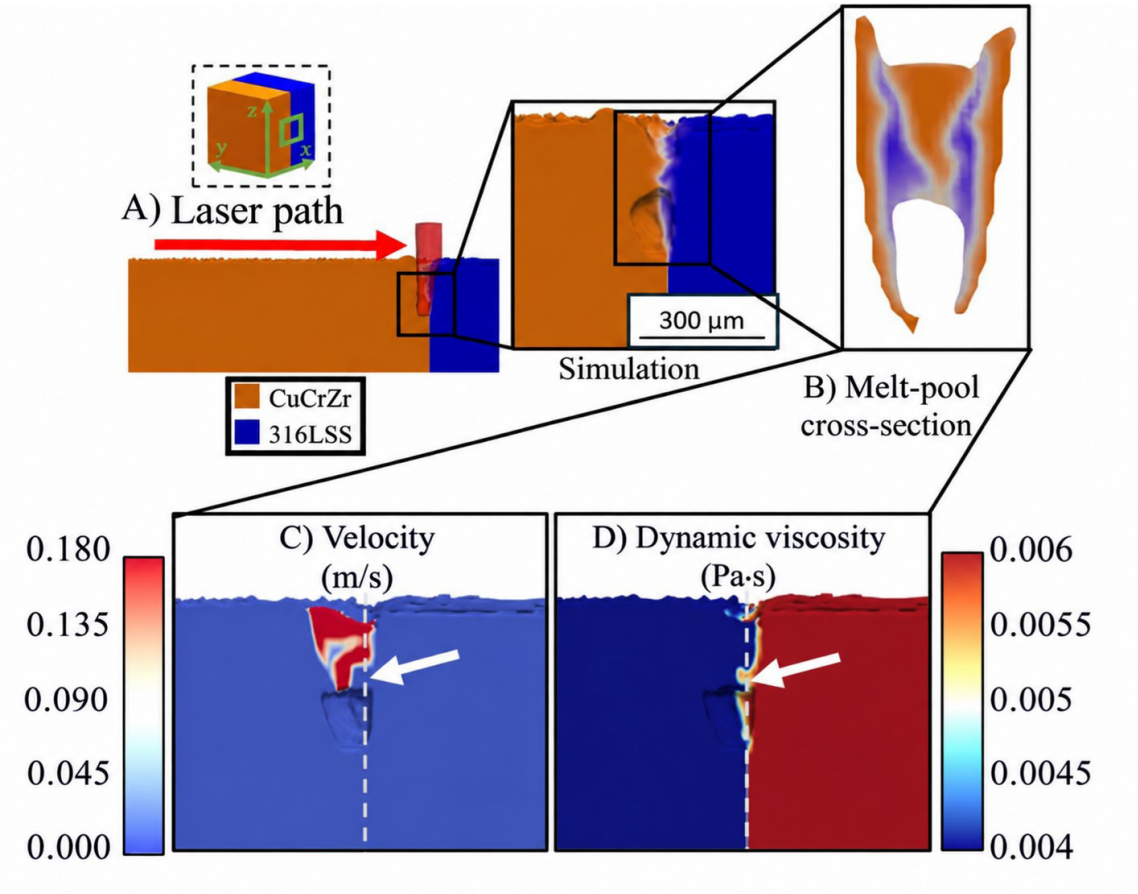


Figure 14. Cross-sectional views of the keyhole collapse as the CuCrZr laser approaches the 316LSS material interface, showing (A) the laser path toward the interface, (B) the melt pool molten material volume fraction, (C) the velocity, and (D) the dynamic viscosity of the melt track during the onset of keyhole collapse. Scale bar: 300 µm.

conductivity 316LSS into high-conductivity CuCrZr, heat is rapidly extracted, suppressing keyholing and stabilizing the melt pool.

The CFD simulations illustrate the relationship between build orientation considerations, melt-pool morphology, and interfacial mixing severity. Interface orientations presenting severe or unstable melt-pool depth and width correspond to experimental locations containing process-specific defects such as keyhole porosity. Conversely, shallow stable melt pools minimize mixing and may be more desirable for material combinations which are susceptible to solidification-based defects because of severe mixing. Overall, the CFD study provides a detailed physics-based understanding of how orientation, laser approach direction, and thermal conductivity differences govern melt-pool morphology development. Furthermore, the results demonstrate that material-specific laser processing conditions can create melt-pool instabilities when transitioning across dissimilar metal interfaces, presenting the need for process adaptation, such as variable power, beam profile, scan speed, scan path, or tailored interface design work,[19] to compensate for predicted melt-pool instability and control interfacial characteristics.

This work demonstrates that successful MM-LPBF processing of highly dissimilar materials is influenced by a dynamic interfacial problem governed by material compatibility, deposition and laser exposure order, thermal asymmetry, melt-pool evolution, and interface geometry. By investigating five discrete CuCrZr-316LSS interface orientations, this study reveals how laser exposure sequence and build orientation contribute to interfacial mixing behavior, defect formation, and microstructural evolution in systems with extreme thermophysical mismatch.

The integrated experimental and CFD analysis showed that interfacial stability is extremely sensitive to local thermal history, where differences in conductivity and

applied VED produce asymmetric melt pool convection, unstable melt-pool behavior, and localized defect accumulation. These findings provide important insight into the current challenges in MM-LPBF of highly dissimilar materials and establish that interface design itself must become a primary process consideration in future MM-LPBF development.

Ongoing and future research efforts should transition beyond distinct binary material systems and explore the implementation of functionally graded, or third-material interlayers specifically engineered to mitigate thermal and metallurgical incompatibilities through tailored alloying. In parallel, advanced *in situ* monitoring techniques capable of capturing melt-pool instability, keyhole fluctuations, and defect initiation in real time will be essential for achieving process reliability. Emerging approaches, such as adaptive beam shaping, spatially tailored energy input, and closed-loop process control, also present promising pathways to stabilize melt-pool dynamics. This work provides a framework for understanding the formation of discrete interfaces in MM-LPBF and represents a major step toward the broader realization of multi-functional, multi-metallic components for advanced engineering applications.

5. Conclusion

This work demonstrates that the bi-metallic interface quality in highly dissimilar MM-LPBF systems is fundamentally governed by interface geometry, orientation, and deposition sequence. The results showed that deposition sequence, interface geometry, and build orientation strongly influence defect formation in CuCrZr-316LSS MM-LPBF systems, with optical microscopy and micro-CT revealing significant variations in keyhole porosity behavior consistent with CFD predictions, which showed that differences in absorptivity, melt-pool velocity, and viscosity between the two materials governed melt-pool instability and process-induced defects. SEM, EDS, and EBSD analyses demonstrated that significant interfacial cracking originated primarily from metallurgical incompatibility within the mixed transition region.

These insights enable prediction of interfacial mixing trends, relative susceptibility to keyhole formation, and the identification of processing conditions that promote stable melt pools in MM-LPBF systems. The results further highlight that successful fabrication of highly dissimilar material combinations will likely require advanced processing strategies beyond conventional parameter optimization in single-material systems, including tailored third-material interlayer alloying approaches to reduce thermophysical incompatibilities. Future advancements in MM-LPBF will also benefit from the implementation of adaptive beam shaping, closed-loop process control, and *in situ* monitoring techniques capable of detecting unstable melt-pool behavior and defect initiation in real time. Overall, the findings presented in this research provide a pathway towards more predictive and, in the future, controllable MM-LPBF processing of thermally and metallurgically dissimilar metallic systems.

List of abbreviations

Abbreviation	Full form
AM	Additive manufacturing
BCC	Body-centered cubic
CFD	Computational fluid dynamics
CT	Computed tomography
CTE	Coefficient of thermal expansion
DEM	Discrete element method
EBSD	Electron backscatter diffraction
EDS	Energy-dispersive X-ray spectroscopy
FCC	Face-centered cubic
FGM-DED	Functionally graded material-directed energy deposition
FWHM	Full width at half maximum
HIP	Hot isostatic pressing
KAM	Kernel average misorientation
LPBF	Laser powder bed fusion
MM-LPBF	Multi-material laser powder bed fusion
SEM	Scanning electron microscopy
SPD	Selective powder deposition
STEM	Scanning transmission electron microscopy
TEM	Transmission electron microscopy
VED	Volumetric energy density
XRD	X-ray diffraction

Acknowledgments

The authors acknowledge Dr. Jennifer Gray and Wesley Auker of the Materials Characterization Laboratory (MCL) at The Pennsylvania State University for their assistance with focused ion beam (FIB) sample preparation and transmission electron microscopy (TEM) data collection. The authors also thank Dr. Timothy Tighe of MCL at Pennsylvania State University for his support with

nanoindentation testing, and Andrew Ross of the Center for Quantitative Imaging at Penn State for assistance with micro-computed tomography (micro-CT) data acquisition.

Funding

The authors acknowledge the Applied Research Laboratory at The Pennsylvania State University for their support through the Walker Graduate Assistantship. This work was partially supported by the National Science Foundation under CMMI-EDSE Award No. 2130694.

Conflict of interest

The authors declare no competing interests related to this work.

Author contributions

Conceptualization: Jacklyn Griffis, Guha Manogharan
Formal analysis: All authors
Investigation: Jacklyn Griffis, Guha Manogharan, Aishwarya Deshpande, Bryan Gong, Kazi Shahed
Methodology: Jacklyn Griffis, Guha Manogharan, Aishwarya Deshpande, Bryan Gong, Kazi Shahed
Writing–original draft: All authors
Writing–review & editing: All authors

Ethics approval and consent to participate

Not applicable.

Consent for publication

Not applicable.

Availability of data

The data that support the findings of this study are available from the corresponding author upon reasonable request.

References

1. Griffis J, Masker A, Schreiber J, Manogharan G. Site-Specific Property Informed Interface Design of Multi-Material Laser Powder Bed Fusion. In: *Volume 1: Additive Manufacturing; Advanced Materials Manufacturing; Biomanufacturing; Life Cycle Engineering*. American Society of Mechanical Engineers; 2024.

   doi: 10.1115/msec2024-125138

2. Griffis JC, Shahed K, Meinert K, Yilmaz B, Lear M, Manogharan G. Multi-material laser powder bed fusion: effects of build orientation on defects, material structure and mechanical properties. *npj Adv Manuf*. 2025;2(1):5.

   doi: 10.1038/s44334-025-00020-5

3. Griffis JC, Shahed KS, Okwudire CE, Manogharan GP. Process Modeling of Multi-Material Laser Powder Bed Fusion. In: Solid Freeform Fabrication. 2023.

   doi: 10.26153/tsw/50998

4. Griffis J, Wang J, Hartman K, *et al.* Advancing multi-material laser powder bed fusion through topology optimized design. *Addit Manuf*. 2026;125:105247.

   doi: 10.1016/j.addma.2026.105247

5. Shaikh A, Griffis J, Stebbins R, *et al.* Towards gradient design of TPMS lattices and laser powder bed fusion processing–Role of laser strategies and lattice thickness. *Manuf Lett*. 2024;41:1046-1054.

   doi: 10.1016/j.mfglet.2024.09.129

6. Shaikh A, Saxena A, Griffis J, Shahed K, Manogharan G. Functionally graded TPMS gyroid structures for additive manufacturing of non-pneumatic tires. *Mater Sci Addit Manuf*. 2024;3(4):5022.

   doi: 10.36922/msam.5022

7. Hartman K, Nguyen-Van S, Griffis J, *et al.* Additive manufacturing of functionally graded thickness in TPMS lattice structures with optimised mechanical strength. *Virtual Phys Prototyp*. 2026;21(1):e2686063.

   doi: 10.1080/17452759.2026.2686063

8. Reichardt A, Shapiro AA, Otis R, *et al.* Advances in additive manufacturing of metal-based functionally graded materials. *Int Mater Rev*. 2021;66(1):1-29.

   doi: 10.1080/09506608.2019.1709354

9. Carroll BE, Otis RA, Borgonia JP, *et al.* Functionally graded material of 304L stainless steel and inconel 625 fabricated by directed energy deposition: Characterization and thermodynamic modeling. *Acta Mater*. 2016;108:46-54.

   doi: 10.1016/j.actamat.2016.02.019

10. Dev Singh D, Arjula S, Raji Reddy A. Functionally Graded Materials Manufactured by Direct Energy Deposition: A review. *Mater Today Proc*. 2021;47:2450-2456.

    doi: 10.1016/j.matpr.2021.04.536

11. Ghanavati R, Mosallanejad MH, Behjat A, *et al.* Multi-material processing of metallic components by direct additive manufacturing methods: technologies, scientific insights, and industrial applications. *Int J Extreme Manuf*. 2026;8(4):042004.

    doi: 10.1088/2631-7990/ae5295

12. Demir AG, Kim J, Caltanissetta F, *et al.* Enabling multi-material gradient structure in laser powder bed fusion. *J Mater Process Technol*. 2022;301:117439.

    doi: 10.1016/j.jmatprotec.2021.117439

13. Kulkarni A, Peddiraju VC, Chatterjee S, Srinivasan D. Effect of Build Geometry and Porosity in Additively Manufactured

CuCrZr. *J Eng Mater Technol*. 2024;146(3).

doi: 10.1115/1.4064003

14. Yu X, Griffis J, Manogharan G, Panesar A. Multi-material additive manufacturing: a computational design perspective. *Virtual Phys Prototyp*. 2025;20(1):e2546671.

doi: 10.1080/17452759.2025.2546671

15. Dongfang K, Fan H, Sui S, *et al.* Effect of Laser Powder Bed Fusion Process Parameters on the Microstructures, Mechanical Properties, and Conductivity of CuCrZr Alloy. *J Materi Eng Perform*. 2024;34(13):13304-13317.

doi: 10.1007/s11665-024-10026-3

16. Morshed-Behbahani K, Aliyu A, Bishop DP, Nasiri A. Additive manufacturing of copper-based alloys for high-temperature aerospace applications: A review. *Mater Today Commun*. 2024;38:108395.

doi: 10.1016/j.mtcomm.2024.108395

17. Cortis D, Pilone D, Grazzi F, *et al.* Functionally graded material via L-PBF: characterisation of multi-material junction between steels (AISI 316L/16MnCr5), copper (CuCrZr) and aluminium alloys (Al-Sc/AlSi10Mg). *Prog Addit Manuf*. 2025;10(4):2455-2472.

doi: 10.1007/s40964-024-00761-3

18. Chueh YH, Hsieh BY, Shih AJ. Interfacial characteristics in multi-material laser powder bed fusion of CuZr/316L stainless steel. *CIRP Ann*. 2024;73(1):145-148.

doi: 10.1016/j.cirp.2024.03.001

19. Mao S, Ren Z, Liu G, Zhang DZ. The effect of processing parameters on the molten pool dynamics during laser powder bed fusion of CuCrZr/316L multi-material. *J Mater Res Technol*. 2024;31:1769-1785.

doi: 10.1016/j.jmrt.2024.06.115

20. Zhai W, Li G, Zhou W. Evaluation of Laser Powder Bed Fusion-Fabricated 316L/CuCrZr Bimetal Joint. *Materials*. 2025;18(7):1434.

doi: 10.3390/ma18071434

21. Jin X, Hoo ZS, Jin C, Xiao Z, Yao L. Microhardness and Tensile Strength Analysis of SS316L/CuCrZr Interface by Laser Powder Bed Fusion. *Materials*. 2024;17(12):2836.

doi: 10.3390/ma17122836

22. Mao S, Yang B, Liu G, Liu G, Zhang Z. Temperature distribution and residual stress evolution at the interface of CuCrZr/316 L multi-material by laser powder bed fusion. *Opt Laser Technol*. 2023;163:109355.

doi: 10.1016/j.optlastec.2023.109355

23. Martendal CP, Esteves PDB, Deillon L, *et al.* Effects of beam shaping on copper-steel interfaces in multi-material laser beam powder bed fusion. *J Mater Process Technol*. 2024;327:118344.

doi: 10.1016/j.jmatprotec.2024.118344

24. Li Z, Kuai Z, Liu B, *et al.* Selective laser melting of 316L–CuCrZr bimetallic structure via In718 transition layer. *J Mater Res Technol*. 2023;25:3819-3834.

doi: 10.1016/j.jmrt.2023.06.196

25. Kuai Z, Li Z, Liu B, Chen Y, Li H, Bai P. Microstructure and mechanical properties of CuCrZr/316L hybrid components manufactured using selective laser melting. *J Alloys Compd*. 2023;955:170103.

doi: 10.1016/j.jallcom.2023.170103

26. Deillon L, Abando Beldarrain N, Li X, Bambach M. Coupling hot isostatic pressing and laser powder bed fusion: A new strategy to manufacture defect-free CuCrZr-316L steel multi-material structures. *Mater Des*. 2024;241:112914.

doi: 10.1016/j.matdes.2024.112914

27. Meyer I, Oel M, Ehlers T, Lachmayer R. Additive manufacturing of multi-material parts – Design guidelines for manufacturing of 316L/CuCrZr in laser powder bed fusion. *Heliyon*. 2023;9(8):e18301.

doi: 10.1016/j.heliyon.2023.e18301

28. Wang Y, Liu B, Tang Q, Huo W, Li Z, Bai Y. Interface microstructure and mechanical properties of selective laser melting-formed CuCrZr alloy for 316 L stainless steel. *Mater Werkst*. 2025;56(1):88-94.

doi: 10.1002/mawe.202400101

29. De Leon E, Riensche A, Bevans BD, Billings C, Siddique Z, Liu Y. A Review of Modeling, Simulation, and Process Qualification of Additively Manufactured Metal Components via the Laser Powder Bed Fusion Method. *J Manuf Mater Process*. 2025;9(1):22.

doi: 10.3390/jmmp9010022

30. Sun Z, Chueh YH, Li L. Multiphase mesoscopic simulation of multiple and functionally gradient materials laser powder bed fusion additive manufacturing processes. *Addit Manuf*. 2020;35:101448.

doi: 10.1016/j.addma.2020.101448

31. Samad SN, Griffis J, Manogharan G, Kouraytem N. Multi-material additive manufacturing of metals: A review of structures and mechanical characteristics. *Eng Sci Addit Manuf*. 2025;1(2):025180010.

doi: 10.36922/ESAM025180010

32. Chen N, Khan HA, Wan Z, *et al.* Microstructural characteristics and crack formation in additively manufactured bimetal material of 316L stainless steel and Inconel 625. *Addit Manuf*. 2020;32:101037.

doi: 10.1016/j.addma.2020.101037

33. Gu H, Wei C, Li L, *et al.* Multi-physics modelling of molten pool development and track formation in multi-track,

multi-layer and multi-material selective laser melting. *Int J Heat Mass Transf*. 2020;151:119458.

doi: 10.1016/j.ijheatmasstransfer.2020.119458

34. Stainless Steel 316L - 1.4404 Data Sheet - thyssenkrupp Materials (UK). Materials UK. Accessed September 27, 2024. https://www.thyssenkrupp-materials.co.uk/stainless-steel-316l-14404.html

35. Eckart TLS Powder Alloys. Eckart NAFTA. Accessed April 21, 2024. https://www.eckart.net/us/en/am/tls

36. Oliver WC, Pharr GM. An improved technique for determining hardness and elastic modulus using load and displacement sensing indentation experiments. *J Mater Res*. 1992;7(6):1564-1583.

doi: 10.1557/jmr.1992.1564

37. Scherrer P. Estimation of the Size and Internal Structure of Colloidal Particles by Means of Röntgen. *Nachrichten Von Ges Wiss Zu Gött*. 1918;2:96-100.

38. Abdel-Rahman AS, Sabry YA. An approach to the micro-strain distribution inside nanoparticle structure. *Int J Non-Linear Mech*. 2024;161:104670.

doi: 10.1016/j.ijnonlinmec.2024.104670

39. Maniammal K, Madhu G, Biju V. X-ray diffraction line profile analysis of nanostructured nickel oxide: Shape factor and convolution of crystallite size and microstrain contributions. *Phys E Low-Dimens Syst Nanostructures*. 2017;85:214-222.

doi: 10.1016/j.physe.2016.08.035

40. Bayat M, Thanki A, Mohanty S, *et al.* Keyhole-induced porosities in Laser-based Powder Bed Fusion (L-PBF) of Ti6Al4V: High-fidelity modelling and experimental validation. *Addit Manuf*. 2019;30:100835.

doi: 10.1016/j.addma.2019.100835

41. Bayat M, Mohanty S, Hattel JH. Multiphysics modelling of lack-of-fusion voids formation and evolution in In718 made by multi-track/multi-layer L-PBF. *Int J Heat Mass Transf*. 2019;139:95-114.

doi: 10.1016/j.ijheatmasstransfer.2019.05.003

42. Trapp J, Rubenchik AM, Guss G, Matthews MJ. In situ absorptivity measurements of metallic powders during laser powder-bed fusion additive manufacturing. *Appl Mater Today*. 2017;9:341-349.

doi: 10.1016/j.apmt.2017.08.006

43. Bonesso M, Lago M, Favero G, *et al.* Analysis and development of CuCrZr alloy fabrication in LPBF: Impact of process parameters and heat treatments on thermo-mechanical properties. *Mater Today Commun*. 2026;50:114618.

doi: 10.1016/j.mtcomm.2026.114618

44. Lopes P, Zafar F, Costa C, *et al.* A comprehensive study of LPBF parameter influence in 316L stainless steel mechanical properties, macrostructure, and printability. *Proc Inst Mech Eng Part J Mater Des Appl*. 2025;239(4):828-847.

doi: 10.1177/14644207241286674

45. Xu L, Zhang Y, Zhao L, Ren W, Han Y. Performance Improvement for the CuCrZr Alloy Produced by Laser Powder Bed Fusion Using the Remelting Process. *Materials*. 2024;17(3):624.

doi: 10.3390/ma17030624

46. Azizi N, Jabari E, Hasanabadi M, Toyserkani E. High-power laser powder bed fusion of Cu–Cr–Zr alloy: A comprehensive study on statistical process optimization, microstructure, and mechanical properties. *J Manuf Process*. 2025;149:931-954.

doi: 10.1016/j.jmapro.2025.06.007

47. Tang X, Chen X, Sun F, *et al.* A study on the mechanical and electrical properties of high-strength CuCrZr alloy fabricated using laser powder bed fusion. *J Alloys Compd*. 2022;924:166627.

doi: 10.1016/j.jallcom.2022.166627

48. Xie H, Tang X, Chen X, *et al.* The effect of build orientations on mechanical and thermal properties on CuCrZr alloys fabricated by laser powder bed fusion. *J Mater Res Technol*. 2023;23:3322-3336.

doi: 10.1016/j.jmrt.2023.01.218

49. Kurdi A, Tabbakh T, Basak AK. Microstructural and Nanoindentation Investigation on the Laser Powder Bed Fusion Stainless Steel 316L. *Materials*. 2023;16(17):5933.

doi: 10.3390/ma16175933

50. Uddin MJ, Ramirez-Cedillo E, Mirshams RA, Siller HR. Nanoindentation and electron backscatter diffraction mapping in laser powder bed fusion of stainless steel 316L. *Mater Charact*. 2021;174:111047.

doi: 10.1016/j.matchar.2021.111047

51. Zafari A, Xia K. Laser powder bed fusion of ultrahigh strength Fe-Cu alloys using elemental powders. *Addit Manuf*. 2021;47:102270.

doi: 10.1016/j.addma.2021.102270

52. Mahmoudiniya M, Hermans MJM, Kestens LAI. Grain boundary susceptibility to liquid metal embrittlement during wire arc additive manufacturing of a bronze/stainless steel bimetallic structure. *Mater Charact*. 2025;224:115058.

doi: 10.1016/j.matchar.2025.115058

53. Nippes EF, Ball DJ. Copper-Contamination Cracking: Cracking Mechanism and Crack Inhibitors. *Weld J*. 1982;61(3).

54. Gan Z, Liu H, Li S, He X, Yu G. Modeling of thermal behavior and mass transport in multi-layer laser additive

manufacturing of Ni-based alloy on cast iron. *Int J Heat Mass Transf*. 2017;111:709-722.

doi: 10.1016/j.ijheatmasstransfer.2017.04.055

55. Curiotto S, Greco R, Pryds NH, Johnson E, Battezzati L. The liquid metastable miscibility gap in Cu-based systems. *Fluid Phase Equilibria*. 2007;256(1-2):132-136.

doi: 10.1016/j.fluid.2006.10.003

56. Wilde G, Willnecker R, Singh RN, Sommer F. The Metastable Miscibility Gap in the System Fe–Cu. *Int J Mater Res*. 1997;88(10):804-809.

doi: 10.3139/ijmr-1997-0151

57. Wen Y, Wu X, Huang A, *et al.* Laser powder bed fusion of immiscible steel and bronze: A compositional gradient approach for optimum constituent combination. *Acta Mater*. 2024;264:119572.

doi: 10.1016/j.actamat.2023.119572

58. Hyer H, Zhou L, Park S, *et al.* Understanding the Laser Powder Bed Fusion of AlSi10Mg Alloy. *Metallogr Microstruct Anal.* 2020;9(4):484-502.

doi: 10.1007/s13632-020-00659-w

59. Wang D, Lv J, Liu Z, *et al.* Interface Optimization, Microstructural Characterization, and Mechanical Performance of CuCrZr/GH4169 Multi-Material Structures Manufactured via LPBF-LDED Integrated Additive Manufacturing. *Materials*. 2025;18(10):2206.

doi: 10.3390/ma18102206

60. Mao S, Zhang DZ, Ren Z, Fu G, Ma X. Effects of process parameters on interfacial characterization and mechanical properties of 316L/CuCrZr functionally graded material by selective laser melting. *J Alloys Compd*. 2022;899:163256.

doi: 10.1016/j.jallcom.2021.163256

61. Tan C, Chew Y, Bi G, *et al.* Additive manufacturing of steel–copper functionally graded material with ultrahigh bonding strength. *J Mater Sci Technol*. 2021;72:217-222.

doi: 10.1016/j.jmst.2020.07.044

62. Livne Z, Munitz A. Characterization of explosively bonded iron and copper plates. *J Mater Sci*. 1987;22(4):1495-1500.

doi: 10.1007/BF01233153

63. Zhang Z, Mativenga P, Huang SQ. Manufacturing, Microstructure, and Mechanics of 316L SS Biomaterials by Laser Powder Bed Fusion. *J Funct Biomater*. 2025;16(8):280.

doi: 10.3390/jfb16080280

64. Zhang S, Wu X, Wang Z, *et al.* Microstructural and Mechanical Property Variations in 316L Stainless Steel Fabricated by Laser Powder Bed Fusion Under High-Density Processing Conditions. *Materials*. 2025;18(16):3899.

doi: 10.3390/ma18163899

65. An SU, Larionov V, Monastryrski V, *et al.* The Thermal Analysis of the Mushy Zone and Grain Structure Changes during Directional Solidification of Superalloys. In: *Superalloys 2000 (Ninth International Symposium)*. TMS; 2000:247-254.

doi: 10.7449/2000/Superalloys_2000_247_254

66. Drezet JM, Ayrault D, Wisniewski J, *et al.* Étude de la sensibilité à la fissuration à chaud d'un alliage CuCrZr au cours du soudage par faisceau d'électrons. *Matér Tech*. 2010;98(4):287-296.

doi: 10.1051/mattech/2010108

67. Ren N, Li J, Zhang R, *et al.* Solute trapping and non-equilibrium microstructure during rapid solidification of additive manufacturing. *Nat Commun*. 2023;14(1):7990.

doi: 10.1038/s41467-023-43563-x

68. Haghdadi N, Breen AJ, Chen H, *et al.* New insights into the character of austenite-ferrite boundaries in an additively manufactured duplex stainless steel. *Scr Mater*. 2024;245:116049.

doi: 10.1016/j.scriptamat.2024.116049

69. Ma J, Song Y, Jiang H, Rong L. Effect of Cu on the Microstructure and Mechanical Properties of a Low-Carbon Martensitic Stainless Steel. *Materials*. 2022;15(24):8849.

doi: 10.3390/ma15248849

70. Banas J, Mazurkiewicz A. The effect of copper on passivity and corrosion behaviour of ferritic and ferritic–austenitic stainless steels. *Mater Sci Eng A*. 2000;277(1-2):183-191.

doi: 10.1016/S0921-5093(99)00530-4

71. Kapoor I, Davis C, Li Z. Effects of residual elements during the casting process of steel production: a critical review. *Ironmak Steelmak*. 2021;48(6):712-727.

doi: 10.1080/03019233.2021.1898869

72. Krawczyk R, Słania J, Golański G, Pfeifer T. Mechanical Properties and Microstructure of Austenite—Ferrite Duplex Stainless Steel Hybrid (Laser + GMAW) and SAW Welded Joint. *Materials*. 2023;16(7):2909.

doi: 10.3390/ma16072909

73. Tao P, Gong J-M, Wang Y-F, Jiang Y, Li Y, Cen W-W. Characterization on stress-strain behavior of ferrite and austenite in a 2205 duplex stainless steel based on nanoindentation and finite element method. *Results Phys*. 2018;11:377-384.

doi: 10.1016/j.rinp.2018.06.023

74. Li X, Gao F, Jiao J, Cao G, Wang Y, Liu Z. Influences of cooling rates on delta ferrite of nuclear power 316H austenitic stainless steel. *Mater Charact*. 2021;174:111029.

doi: 10.1016/j.matchar.2021.111029

75. Gao L, Chen Y, Zhang X, Agnew SR, Chuang AC, Sun T.

Evolution of dislocations during the rapid solidification in additive manufacturing. *Nat Commun*. 2025;16(1):4696.

doi: 10.1038/s41467-025-59988-5

76. Liu W, Shen S, Meng J, *et al.* Mechanical field assisted additive manufacturing of ultrahigh strength aluminum alloy. *Int J Extreme Manuf*. 2025;7(4):045008.

doi: 10.1088/2631-7990/adbb95

77. Abbaschian R, Reed-Hill RE. *Physical Metallurgy Principles*. Cengage Learning; 2008. https://books.google.com/books/about/Physical_Metallurgy_Principles.html?id=iYUGAAAAQBAJ

78. Dieter GE. *Mechanical Metallurgy*. McGraw-Hill Book Company; 1961. https://books.google.com/books/about/MECHANICAL_METALLURGY.html?id=aztpTSdVSAQC

79. Sprouster DJ, Streit Cunningham W, Halada GP, *et al.* Dislocation microstructure and its influence on corrosion behavior in laser additively manufactured 316L stainless steel. *Addit Manuf*. 2021;47:102263.

doi: 10.1016/j.addma.2021.102263

80. Navarre C, Van Petegem S, Schlenger L, *et al.* Monitoring of laser-induced fast recrystallization in SS-316L through synchrotron X-ray diffraction. *Mater Des*. 2024;238:112628.

doi: 10.1016/j.matdes.2023.112628

81. Hall EO. The Deformation and Ageing of Mild Steel: III Discussion of Results. *Proc Phys Soc Sect B*. 1951;64(9):747-753.

doi: 10.1088/0370-1301/64/9/303

82. Zhang X, Fang T, Saniie J, Bakhtiari S, Heifetz A. Unsupervised learning-enabled pulsed infrared thermographic microscopy of subsurface defects in stainless steel. *Sci Rep*. 2024;14(1):14865.

doi: 10.1038/s41598-024-64214-1

83. Aurubis. Material Datasheet for CuCrZr. https://www.aurubis.com/dam/jcr:d6d50d64-69d6-4742-821d-8fb8b48c9044/cucrzr-c18160-pna-372_en.pdf

84. Griffis J, Shaikh A, Gong B, Jacob A, Schreiber J, Manogharan G. Mechanical interlocking as a design-driven approach to strengthen multi-material laser powder bed fusion interface. *Mater Des*. 2026;271:117097.

doi: 10.1016/j.matdes.2026.117097

Supplemental information

Video S1. Simulation: Steel toward CuCrZr-CuCrZr over steel diagonal interface

Video S2. Simulation: CuCrZr toward Steel-CuCrZr over steel diagonal interface

Video S3. Simulation: Steel toward CuCrZr-Steel over CuCrZr diagonal interface

Video S4. Simulation: CuCrZr toward Steel-Steel over CuCrZr diagonal interface

Video S5. Simulation: Steel over CuCrZr horizontal interface

Video S6. Simulation: CuCrZr over steel horizontal interface

Video S7. Simulation: Steel toward CuCrZr vertical interface

Video S8. Simulation: CuCrZr toward steel vertical interface